Vibrational Spectroscopy of C_{60}

José Menéndez and John B. Page

Department of Physics and Astronomy
Arizona State University
Tempe, AZ 85287–1504 USA

The fullerene era was started in 1985 with the discovery of the stable C_{60} cluster and its interpretation as a cage structure with the familiar shape of a soccer ball [1]. An explosive growth in fullerene research was triggered in 1990 by the development of a method to produce fullerenes in bulk quantities [2]. Subsequently, the structural, electronic, and vibrational properties of many fullerenes have been studied in detail. The importance and potential of this new class of materials is exemplified by the discovery of intermediate-temperature superconductivity in doped C_{60} [3]. Carbon nanotubes, a novel form of carbon which combines the properties of graphite and fullerenes, were discovered in 1991 [4]. Because of their intriguing properties and potential for applications, nanotubes are currently the subject of very intense research. Polymerization of C_{60} molecules, particularly by photoexcitation [5] but by several other techniques as well, also results in a variety of interesting new structures, which contain both 4-coordinated and 3-coordinated carbon atoms [6]. The burgeoning field of fullerene research has been reviewed by several authors [7–12], most notably by *Dresselhaus* et al. [11] in an extensive monograph that appeared in 1996.

In spite of the rapidly increasing interest in new forms of fullerenes, icosahedral C_{60}, the "most beautiful molecule" [13], remains the focus of vigorous research as the prototype fullerene system. The present chapter concerns the vibrational structure of C_{60} and the efforts to unravel its details using spectroscopic techniques. This remains a work in progress, but we hope to show that a look at the existing body of experimental and theoretical research from the broader perspective of an extended article provides a deeper understanding of the vibrational properties of C_{60}.

1 Vibrations in C_{60}

Several reviews have appeared on the vibrational structure of C_{60}, with emphasis on Raman and infrared spectroscopy [11,14,15]. We have tried to limit the overlap with these works by emphasizing recent developments and providing sufficient theoretical detail to facilitate the critical evaluation of comparisons between measured and calculated spectra. No attempt is made to

provide complete bibliographic references on the topics discussed, as these are readily assembled, e.g. via the reviews cited above and by following up references in the work we discuss. Accordingly, we have tried to select those references which most usefully illustrate the points under consideration.

We begin in Sect. 1.1 with a brief introduction to relevant aspects of molecular vibrations, followed by a discussion in Sect. 1.2 of symmetry properties and spectroscopic selection rules for isolated icosahedral C_{60} molecules. Section 1.3 concerns symmetry-lowering perturbations arising from the intermolecular interactions in condensed phases and from the presence of carbon isotopes. Theoretical approaches used to calculate the vibrational frequencies and eigenvectors of C_{60} are discussed in Sect. 1.4. Also given there is our preferred frequency assignment for all of the vibrational modes in icosahedral C_{60}. The frequencies are based on data from a wide variety of vibrational spectroscopies and are compared with representative theoretical results. The experimental data are detailed in Sect. 2, with special emphasis on the spectroscopy of "silent" modes, i.e. those which are neither infrared nor Raman active in first order. Finally, Sects. 3 and 4 discuss infrared and Raman intensities. The development of accurate models to reproduce these intensities is an important prerequisite for the understanding of the much more complicated spectra of higher fullerenes, nanotubes and polymers.

1.1 Theoretical Basis

At a fundamental level, the vibrational properties of solids or molecules such as C_{60} derive from the many-electron states, as do the quantities which determine the spectroscopic coupling strengths, e.g. Raman polarizability derivatives and IR effective charges. The last decade has seen rapid advances in the development of numerous "first-principles" techniques for the practical calculation of electronic, vibrational, and structural properties from a unified many-electron point of view; some of these techniques will figure into our subsequent discussion.

For nonmetallic systems whose vibrational and electronic transition energies are well-separated, the eigenstates may be described within the adiabatic (i.e. Born-Oppenheimer) approximation as products of coupled electronic and vibrational states

$$\Psi_{n\nu}(\boldsymbol{x},\boldsymbol{u}) = \phi_n(\boldsymbol{x},\boldsymbol{u})\psi_{n\nu}(\boldsymbol{u}), \tag{1}$$

where n and ν are the electronic and vibrational quantum numbers, respectively. The many-electron states $\phi_n(\boldsymbol{x},\boldsymbol{u})$ depend parametrically on the atoms' displacements, represented collectively by $\boldsymbol{u}$, and on the electronic coordinates $\boldsymbol{x}$. They are eigenfunctions of the many-electron problem for fixed atomic configuration $\boldsymbol{u}$:

$$[T_E + V_{EE}(\boldsymbol{x}) + V_{EN}(\boldsymbol{x},\boldsymbol{u}) + V_{NN}(\boldsymbol{u})]\phi_n(\boldsymbol{x},\boldsymbol{u}) = E_n(\boldsymbol{u})\phi_n(\boldsymbol{x},\boldsymbol{u}), \tag{2}$$

where T_E is the electronic kinetic energy operator and the nuclear-nuclear potential energy $V_{NN}(\boldsymbol{u})$ has been included. The vibrations are then determined by taking the effective potential energy function for the atoms to be the many-electron ground state energy eigenvalue: $V(\boldsymbol{u}) \equiv E_0(\boldsymbol{u})$. This assumes that the system remains in its many-electron ground state as the atoms move.

The minimum of V defines the atomic equilibrium configuration. The atoms' displacements from equilibrium are given by the $3N \times 1$ configuration space vector $\boldsymbol{u} \equiv \{u(\ell\alpha)\}$, where $\ell = 1, \ldots, N$ labels sites and α denotes x, y, or z. Within the harmonic approximation, V is quadratic in the displacements:

$$V = \frac{1}{2} \sum_{\ell\alpha, \ell'\alpha'} \Phi(\ell\alpha, \ell'\alpha') u(\ell\alpha) u(\ell'\alpha') = \frac{1}{2} \tilde{\boldsymbol{u}} \boldsymbol{\Phi} \boldsymbol{u}, \tag{3}$$

where $\boldsymbol{\Phi} \equiv \{\Phi(\ell\alpha, \ell'\alpha') = [\partial^2 V / \partial u(\ell\alpha) \partial u(\ell'\alpha')]_0\}$ is the $3N \times 3N$ harmonic force constant matrix, with the derivatives evaluated at the equilibrium configuration $\boldsymbol{u} = \boldsymbol{0}$. The tilde denotes the transpose, and the zero of potential energy is taken at the equilibrium configuration. The vibrational Hamiltonian is then

$$H = \frac{1}{2} (\tilde{\boldsymbol{p}} \boldsymbol{M}^{-1} \boldsymbol{p} + \tilde{\boldsymbol{u}} \boldsymbol{\Phi} \boldsymbol{u}), \tag{4}$$

where the diagonal matrix $\boldsymbol{M} \equiv \{m(\ell) \delta_{\ell\ell'} \delta_{\alpha\alpha'}\}$ contains the atoms' masses and $\boldsymbol{p} \equiv \{p(\ell\alpha)\}$ contains their momenta.

The normal mode frequencies and displacement patterns are obtained by solving the eigenvalue problem

$$(\boldsymbol{\Phi} - \omega_f^2 \boldsymbol{M}) \boldsymbol{\chi}(f) = 0, \tag{5}$$

where $f = 1, \ldots, 3N$ labels the modes. Since both the force constant and mass matrices are real and symmetric, the eigenvectors may be taken as complete and orthonormal with respect to $\boldsymbol{M}$:

$$\sum_{f=1}^{3N} \boldsymbol{M} \boldsymbol{\chi}(f) \tilde{\boldsymbol{\chi}}(f) = \boldsymbol{I}, \tag{6}$$

and

$$\tilde{\boldsymbol{\chi}}(f) \boldsymbol{M} \boldsymbol{\chi}(f') = \delta_{ff'}. \tag{7}$$

The $3N$ normal coordinates $\{d_f\}$ and their conjugate momenta $\{p_f\}$ are linearly related to the atomic displacements and momenta through

$$\boldsymbol{u} = \sum_f \boldsymbol{\chi}(f) d_f \tag{8}$$

and

$$\boldsymbol{p} = \boldsymbol{M} \sum_f \boldsymbol{\chi}(f) p_f. \tag{9}$$

When these equations are substituted into (4) and the eigenvalue equation (5) and orthonormality condition (7) are used, the Hamiltonian reduces to that for a sum of independent harmonic oscillators

$$H = \frac{1}{2} \sum_f (p_f^2 + \omega_f^2 d_f^2). \tag{10}$$

The normal coordinate transformation is valid within either a classical or quantum mechanical treatment of the vibrational problem. In the former case the normal coordinates and their conjugate momenta satisfy Hamilton's equations, leading to $\ddot{d}_f + \omega_f^2 d_f = 0$. In the quantum case, these quantities are operators satisfying commutation relations $[d_f, p_{f'}] = i\hbar\delta_{ff'}$, and the vibrational Hamiltonian may be reexpressed in the familiar form

$$H = \sum_f \hbar\omega_f (a_f^\dagger a_f + 1/2), \tag{11}$$

where $a_f \equiv (2\hbar\omega_f)^{-1/2}(p_f - i\omega_f d_f)$ is the annihilation operator for mode f. The eigenenergies are then $E_{\{n_f\}} = \sum_f \hbar\omega_f (n_f + \frac{1}{2})$, with $n_f = 0, 1, 2, \ldots$ counting the number of quanta $\hbar\omega_f$ in mode f.

In either the quantum or classical description, the key physical quantities are the mode frequencies ω_f and corresponding displacement patterns $\boldsymbol{\chi}(f) = \{\chi(\ell\alpha|f)\}$, obtained by solving the eigenvalue problem (5). For fullerenes, one typically solves this problem directly, using force constants obtained from phenomenological potential models or from first-principles techniques; both types of calculations will play a role in this chapter.

1.2 Symmetry and Selection Rules

The high symmetry of an isolated, isotopically pure C_{60} molecule in its equilibrium configuration imposes very strong constraints on the form of the normal mode displacement patterns. All 60 sites are symmetry-equivalent, and the point group is the full icosahedral group I_h, consisting of 120 operations. These are the 60 proper symmetry operations of a regular icosahedron, together with each of these operations followed by the inversion. The mode displacement patterns are basis functions for irreducible representations of I_h; that is, they transform under a symmetry operation r as

$$\boldsymbol{\mathcal{R}}\boldsymbol{\chi}(n,i) = \sum_{j=1}^{l_n} \Gamma_{ji}^n(r)\boldsymbol{\chi}(n,j), \tag{12}$$

where the mode label has been split $(f) \rightarrow (n,i)$, with n labeling the irreducible representation and i denoting the partner within the representation. The $3N \times 3N$ matrix $\boldsymbol{\mathcal{R}}$ is the configuration-space version of the symmetry operator r, and $\boldsymbol{\Gamma}^n(r)$ denotes the corresponding irreducible representation matrix, of dimensionality l_n. Owing to the inversion symmetry in C_{60}, the displacement patterns are either invariant under inversion (even modes), or change sign (odd modes). There are 10 irreducible representations of I_h. By reducing the 180-dimensional representation generated by transforming the basis formed from three orthogonal unit vectors on each atom, one can *a priori* predict the mode symmetry types. It is found that the number of linearly independent times each irreducible representation appears is $2(A_g)$, $1(A_u)$, $4(T_{1g})$, $5(T_{1u})$, $4(T_{3g})$, $5(T_{3u})$, $6(G_g)$, $6(G_u)$, $8(H_g)$, and $7(H_u)$. The notation is that of *Weeks* and *Harter* [16], who provide a detailed account of the icosahedral group and its application to the harmonic vibrations of C_{60}. The irreducible representations of types A, T, G, and H are of dimensionalities 1, 3, 4, and 5, respectively, these giving the degeneracies, while the g and u subscripts specify the representations for even and odd modes. The six zero-frequency modes corresponding to rigid translations and rotations account for one appearance each of T_{1u} and T_{1g}, respectively, and when account is taken of the dimensionalities of the remaining irreducible representations, it is seen that there are just 46 distinct frequencies among the 174 vibrational modes.

The high symmetry of a C_{60} molecule also severely restricts the number of spectroscopically active modes in IR absorption and Raman scattering, particularly in first-order processes, i.e. those involving a single vibrational quantum. For absorption, the coupling is through the dipole moment vibrationally induced in the system. In particular, within the adiabatic and dipole approximations, the interaction between a molecule and an external electric field is $-\vec{\mu}(\boldsymbol{u}) \cdot \vec{E} \exp(-i\omega t)$, where $\vec{\mu}(\boldsymbol{u})$ is the expectation value of the total dipole moment in the molecule for a fixed atomic configuration $\boldsymbol{u}$:

$$\vec{\mu}(\boldsymbol{u}) = \sum_{\ell} q_\ell \vec{u}(\ell) + \int d^3x \; \phi_0^*(\boldsymbol{x}, \boldsymbol{u}) \sum_e q_e \vec{x}_e \; \phi_0(\boldsymbol{x}, \boldsymbol{u}). \tag{13}$$

The arrows denote 3-D Cartesian vectors, q_ℓ is the nuclear charge on atom ℓ, the sums are over all of the atoms and electrons, and the expectation value is taken with respect to the electronic coordinates. Physically, the second term describes the electronic charge redistribution induced by atomic motion. Expanding $\vec{\mu}(\boldsymbol{u})$ in powers of the atomic displacements and using (8) to express the result in terms of the normal coordinates gives

$$\vec{\mu}(\boldsymbol{u}) = \sum_f \vec{\mu}_f d_f + \frac{1}{2} \sum_{ff'} \vec{\mu}_{ff'} \; d_f d_{f'} + \cdots , \tag{14}$$

where it is assumed that the system has no permanent dipole moment. The first two coefficients are given by

$$\vec{\mu}_f = \sum_{\ell\alpha} \left[\frac{\partial \vec{\mu}(\boldsymbol{u})}{\partial u(\ell\alpha)} \right]_0 \chi(\ell\alpha|f) \tag{15}$$

and

$$\vec{\mu}_{ff'} = \sum_{\ell\alpha,\ell'\alpha'} \left[\frac{\partial^2 \vec{\mu}(\boldsymbol{u})}{\partial u(\ell\alpha)\partial u(\ell'\alpha')} \right]_0 \chi(\ell\alpha|f)\ \chi(\ell'\alpha'|f'). \tag{16}$$

Within standard linear response theory and the harmonic approximation, the terms in (14) lead to absorption involving one, two, ... vibrational quanta, respectively. Specifically, for a sample containing C molecules per unit volume, the first-order contribution to the absorption is given by

$$A(\omega) = \frac{2\pi^2 C}{3cn} \sum_f |\vec{\mu}_f|^2 \delta(\omega - \omega_f), \tag{17}$$

where n is the medium's refractive index, and an orientational average has been performed. Local field effects have not been included. This harmonic approximation result is independent of the temperature. In practice, the delta function absorption lines are broadened phenomenologically, e.g. as Lorentzians. The integrated absorption strength of a mode f is given by the square of the dipole moment derivative $\vec{\mu}_f$, which according to (14) is the mode's effective charge.

Again within the harmonic approximation, the second-order dipole moment coefficients $\vec{\mu}_{ff'}$ give rise to temperature-dependent sum and difference absorption involving two modes. Sum and difference absorption can also result from the linear term in (14), provided that cubic anharmonicity is present; in this case a virtually excited IR active mode decays anharmonically into the two final state vibrational quanta. Reference [17] designates these two mechanisms for two-quantum absorption as "electrical" and "mechanical," respectively.

The IR selection rules derive from the transformation properties of the dipole moment operator $\vec{\mu}(\boldsymbol{u})$ under symmetry operations. We now summarize the standard group theoretic argument for first-order absorption. It is useful to write the β-component of (15) compactly as

$$\mu_{\beta,f} = \tilde{\boldsymbol{\mu}}_\beta \boldsymbol{\chi}(f), \tag{18}$$

where $\boldsymbol{\mu}_\beta \equiv \{\mu_\beta(\ell\alpha) = [\partial\mu_\beta/\partial u(\ell\alpha)]_0\}$ is the $3N \times 1$ vector of real-space effective charges describing the β-component of the dipole moment. It is straightforward to show that if $\boldsymbol{r} = \{r_{\alpha\alpha'}\}$ is the 3×3 Cartesian matrix for a symmetry operation r, the vectors $\boldsymbol{\mu}_\beta$ transform according to

$$\boldsymbol{\mathcal{R}}\boldsymbol{\mu}_\beta = \sum_{\beta'=1}^{3} r_{\beta'\beta}\boldsymbol{\mu}_{\beta'}; \tag{19}$$

that is, $\boldsymbol{\mu}_x$, $\boldsymbol{\mu}_y$, and $\boldsymbol{\mu}_z$ are basis functions for the representation $\boldsymbol{r}$. For an arbitrary system, this representation would generally be reducible, and in view of (18) and the standard group theory basis function orthogonality theorem [18], $\vec{\mu}_f$ will vanish whenever mode f belongs to an irreducible representation not contained in $\boldsymbol{r}$. For the full icosahedral group, $\boldsymbol{r}$ is just the irreducible representation T_{1u}. Hence only T_{1u} modes can be first-order IR active in pure C_{60}.

For two-quantum absorption, the selection rules for either the second-order dipole moment mechanism (16) or the first-order dipole moment plus cubic anharmonicity mechanism are the same: two modes f and f' cannot be second-order active unless their direct product representation $\boldsymbol{\Gamma}^f \times \boldsymbol{\Gamma}^{f'}$ includes the representation $\boldsymbol{r}$. For pure C_{60}, the resulting possible combination mode symmetry types are listed in Table 1.

Table 1. Symmetry-allowed second-order combinations for infrared absorption and off-resonance Raman scattering, under the full icosahedral point group (I_h). The IR- and Raman-allowed combinations are denoted by I and R, respectively. Adapted from [70]

	Even parity modes					Odd parity modes				
	A_g	T_{1g}	T_{3g}	G_g	H_g	A_u	T_{1u}	T_{3u}	G_u	H_u
A_g	R				R		I			
T_{1g}		R	R	R	R	I	I			I
T_{3g}		R	R	R	R				I	I
G_g		R	R	R	R			I	I	I
H_g	R	R	R	R	R		I	I	I	I
A_u		I				R				R
T_{1u}	I	I			I		R	R	R	R
T_{3u}				I	I		R	R	R	R
G_u			I	I	I		R	R	R	R
H_u		I	I	I	I	R	R	R	R	R

For Raman scattering, we focus on the off-resonance case, when the incident visible photon energy $\hbar\omega_L$ is well below that of any electronic transitions. The relevant quantity is then the system's electronic polarizability $\mathcal{P}_{\alpha\beta}(\omega_L, \boldsymbol{u})$ for fixed atomic configuration $\boldsymbol{u}$, given by

$$\mathcal{P}_{\alpha\beta}(\omega_L, \boldsymbol{u}) = \hbar^{-1} \sum_n \left[\frac{D_\alpha^{0n}(\boldsymbol{u}) D_\beta^{n0}(\boldsymbol{u})}{\omega_{n0}(\boldsymbol{u}) - \omega_L} + \frac{D_\beta^{on}(\boldsymbol{u}) D_\alpha^{n0}(\boldsymbol{u})}{\omega_{n0}(\boldsymbol{u}) + \omega_L} \right]. \tag{20}$$

Here, the electronic transition dipole matrix elements are

$$\vec{D}^{0n}(\boldsymbol{u}) = \int d^3x \, \phi_0^*(\boldsymbol{x}, \boldsymbol{u}) \sum_e q_e \vec{x}_e \, \phi_n(\boldsymbol{x}, \boldsymbol{u}), \tag{21}$$

and $\omega_{n0}(\boldsymbol{u})$ denotes the frequency of electronic transitions $0 \rightarrow n$, for fixed $\boldsymbol{u}$. Note that $\mathcal{P}_{\alpha\beta}(\omega_L, \boldsymbol{u}) = \mathcal{P}^*_{\beta\alpha}(\omega_L, \boldsymbol{u})$, so that the real and imaginary parts of this quantity are, respectively, symmetric and antisymmetric in $\alpha\beta$. For scattered light frequency ω_S, the photon differential scattering cross-section is then [19]

$$\left(\frac{d^2\sigma}{d\Omega d\omega}\right)_{\eta'\eta} = \frac{\omega_L \omega_S^3}{2\pi c^4} \sum_{\alpha\beta\gamma\lambda} \eta'_\alpha \eta_\beta \eta'_\gamma \eta_\lambda \int_{-\infty}^{\infty} dt\ \exp(-it\omega) \times \langle \mathcal{P}^*_{\alpha\beta}(\omega_L, \boldsymbol{u}; t) \mathcal{P}_{\gamma\lambda}(\omega_L, \boldsymbol{u}) \rangle, \tag{22}$$

where $\omega \equiv \omega_S - \omega_L$, and η' and η are the polarization directions of the scattered and incident light, respectively. The brackets denote a thermal average, and $\mathcal{P}^*_{\alpha\beta}(\omega_L, \boldsymbol{u}; t) \equiv \exp(itH/\hbar)\mathcal{P}^*_{\alpha\beta}(\omega_L, \boldsymbol{u}) \exp(-itH/\hbar)$, where H is the vibrational hamiltonian. Similar to the discussion below (14), expansion of $\mathcal{P}_{\alpha\beta}(\omega_L, \boldsymbol{u})$ in the atomic displacements and the use of (8) give

$$\mathcal{P}_{\alpha\beta}(\omega_L, \boldsymbol{u}) = \sum_f P_{\alpha\beta,f} d_f + \frac{1}{2} \sum_{ff'} P_{\alpha\beta,ff'}\ d_f d_{f'} + \cdots . \tag{23}$$

The first-order coefficients are

$$P_{\alpha\beta,f} = \sum_{\ell\gamma} P_{\alpha\beta}(\ell\gamma) \chi(\ell\gamma|f) = \tilde{\boldsymbol{P}}_{\alpha\beta} \boldsymbol{\chi}(f), \tag{24}$$

where the $3N \times 1$ vector $\boldsymbol{P}_{\alpha\beta} \equiv \{P_{\alpha\beta}(\ell\gamma) = [\partial \mathcal{P}_{\alpha\beta}(\omega_L, \boldsymbol{u})/\partial u(\ell\gamma)]_0\}$ contains the real-space electronic polarizability derivatives. Within the harmonic approximation, the use of the linear term of (23) in (22) yields the cross-section for first-order Stokes scattering at frequency shift ω as

$$\left(\frac{d^2\sigma}{d\Omega d\omega}\right)^{1,\mathrm{Stokes}}_{\eta'\eta} = \frac{\hbar\omega_L}{2c^4} \sum_{f=1}^{3N} \frac{(\omega_L - \omega_f)^3 (\langle n(\omega_f)\rangle + 1)}{\omega_f} \times \left| \sum_{\alpha\beta} \eta'_\alpha \eta_\beta P_{\alpha\beta,f} \right|^2 \delta(\omega + \omega_f), \tag{25}$$

where $\langle n(\omega_f)\rangle = [\exp(\hbar\omega_f/k_B T) - 1]^{-1}$ is the thermal average occupation number of mode f at temperature T. This result is for a single molecule and includes no media or local field corrections. Although the frequency shift of the light is negative for Stokes scattering, we will follow the standard convention and refer to $|\omega|$ as the Raman shift.

The transformation properties of the real-space electronic polarizability derivatives $\boldsymbol{P}_{\alpha\beta}$ under symmetry operations yield the Raman selection rules. The presence of two Cartesian indices leads to a generalization of the earlier dipole moment derivative transformation property (19), namely

$$\boldsymbol{\mathcal{R}} \boldsymbol{P}_{\alpha\beta} = \sum_{\alpha'\beta'} (\boldsymbol{r} \times \boldsymbol{r})_{\alpha'\beta',\alpha\beta} \boldsymbol{P}_{\alpha'\beta'}. \tag{26}$$

Here $(\boldsymbol{r}\times\boldsymbol{r})_{\alpha'\beta',\alpha\beta} \equiv r_{\alpha'\alpha}r_{\beta'\beta}$ is an element of the 9-dimensional direct product representation $\boldsymbol{r}\times\boldsymbol{r}$. For the full icosahedral group, this is the reducible representation $T_{1u}\times T_{1u}$, and it decomposes into the irreducible representations A_g, T_{1g}, and H_g. Again invoking the standard group theory orthogonality theorem for basis functions, we see that the right-hand side of (24) vanishes whenever f does not belong to one of these irreducible representations.

One can go further by decomposing the direct product representation $\boldsymbol{r}\times\boldsymbol{r}$ into its symmetric and antisymmetric components, the elements of which are given by $(\boldsymbol{r}\times\boldsymbol{r})^{s,a}_{\alpha'\beta',\alpha\beta} \equiv r_{\alpha'\alpha}r_{\beta'\beta} \pm r_{\beta'\alpha}r_{\alpha'\beta}$, with the plus sign referring to the symmetric component. For $(\boldsymbol{r}\times\boldsymbol{r})^s$, the indices are restricted according to $\alpha' \le \beta'$ and $\alpha \le \beta$, and likewise for $(\boldsymbol{r}\times\boldsymbol{r})^a$, except that the equality is removed. Thus the symmetric and antisymmetric components of $(\boldsymbol{r}\times\boldsymbol{r})$ are 6-dimensional and 3-dimensional, respectively. It is straightforward to show that the combinations $\{\boldsymbol{P}_{\alpha\beta} \pm \boldsymbol{P}_{\beta\alpha}\}$ are basis functions for $(\boldsymbol{r}\times\boldsymbol{r})^{s,a}$. Since the real and imaginary parts of $\boldsymbol{P}_{\alpha\beta}$ are symmetric and antisymmetric in $\alpha\beta$, respectively, the real part is a basis function for $(\boldsymbol{r}\times\boldsymbol{r})^s$, whereas the imaginary part is a basis function for $(\boldsymbol{r}\times\boldsymbol{r})^a$. For the full icosahedral group, the symmetric component of $T_{1u}\times T_{1u}$ contains A_g and H_g, whereas the antisymmetric component is T_{1g}. For off-resonance Raman scattering, it is customary to use the static limit $\omega_L = 0$ in the electronic polarizability, in which case (20) shows that the antisymmetric part of the polarizability vanishes identically. Then only the A_g and H_g modes of C_{60} may be first-order Raman active. For $\omega_L \neq 0$, (20) again leads to this result provided the electronic eigenfunctions are purely real. On the other hand, if complex eigenfunctions cannot be ruled out and $\omega_L \neq 0$, the three T_{1g} modes are, in principle, first-order allowed in off-resonance Raman scattering.

Equation (25) applies to a molecule with a fixed orientation; the indices $\alpha\beta$ refer to axes fixed in the scatterer. It is straightforward to determine the forms of the polarizability derivatives $\{P_{\alpha\beta,f} \to P_{\alpha\beta,(n,i)}\}$ for the first-order Raman active modes, where the mode index f has again been replaced by (n,i), with n labeling the irreducible representation and i the partner. This is conveniently done using projection operator techniques, by determining the forms of the ℓ_n matrices $\sum_r \Gamma^n_{ki}(r)\tilde{\boldsymbol{r}}\boldsymbol{A}\boldsymbol{r}$ for $i = 1,\ldots,\ell_n$ and k held fixed, where $\boldsymbol{A}$ is an arbitrary 3×3 trial matrix and the sum is over all symmetry operations. The results for I_h are given in Table 2. For randomly oriented molecules, i.e. C_{60} in solution, one should average over all orientations. For the common cases of 0°, 90°, and 180° scattering geometries, this leads to the standard results in terms of Placzek invariants [20]. These quantities are $G^0 = \frac{1}{3}|P_{xx}+P_{yy}+P_{zz}|^2$, $G^s = \frac{1}{3}[|P_{xx}-P_{yy}|^2 + |P_{xx}-P_{zz}|^2 + |P_{yy}-P_{zz}|^2] + \frac{1}{2}[|P_{xy}+P_{yx}|^2 + |P_{xz}+P_{zx}|^2 + |P_{yz}+P_{zy}|^2]$, and $G^a = \frac{1}{2}[|P_{xy}-P_{yx}|^2 + |P_{xz}-P_{zx}|^2 + |P_{yz}-P_{zy}|^2]$. If $I_\perp$ and $I_\parallel$ are the scattered intensities with polarization perpendicular and parallel to that of the incident light, the depolarization ratio is $\rho = I_\perp/I_\parallel = (3G^s+5G^a)/(10G^0+4G^s)$, and the total

Table 2. Forms of the polarizability derivative tensors for first-order Raman active modes under icosahedral symmetry. The T_{1g} contributions vanish in either the static limit $\omega_L = 0$ or whenever the electronic eigenfunctions are purely real. These forms were obtained via the projection operator technique described on page 9, using the irreducible representation matrices given by *Weeks* and *Harter* [16]. The z axis is a 5-fold axis, and the yz plane is a reflection plane

A_g	$\begin{pmatrix} a & 0 & 0 \\ 0 & a & 0 \\ 0 & 0 & a \end{pmatrix}$				
H_g	$\begin{pmatrix} b & 0 & 0 \\ 0 & b & 0 \\ 0 & 0 & -2b \end{pmatrix}$	$\begin{pmatrix} \sqrt{3}b & 0 & 0 \\ 0 & -\sqrt{3}b & 0 \\ 0 & 0 & 0 \end{pmatrix}$	$\begin{pmatrix} 0 & \sqrt{3}b & 0 \\ \sqrt{3}b & 0 & 0 \\ 0 & 0 & 0 \end{pmatrix}$	$\begin{pmatrix} 0 & 0 & 0 \\ 0 & 0 & \sqrt{3}b \\ 0 & \sqrt{3}b & 0 \end{pmatrix}$	$\begin{pmatrix} 0 & 0 & -\sqrt{3}b \\ 0 & 0 & 0 \\ -\sqrt{3}b & 0 & 0 \end{pmatrix}$
Partner	1	2	3	4	5
T_{1g}	$\begin{pmatrix} 0 & c & 0 \\ -c & 0 & 0 \\ 0 & 0 & 0 \end{pmatrix}$	$\begin{pmatrix} 0 & 0 & 0 \\ 0 & 0 & c \\ -c & 0 & 0 \end{pmatrix}$	$\begin{pmatrix} 0 & 0 & -c \\ 0 & 0 & 0 \\ c & 0 & 0 \end{pmatrix}$		
Partner	1	2	3		

scattering is $I_{\text{total}} = I_{\parallel} + I_{\perp} \propto 10G^0 + 7G^s + 5G^a$. From the results of Table 2, the depolarization ratios for first-order scattering by A_g and H_g modes are 0 and 3/4, respectively, while if T_{1g} scattering occurs, it is predicted to have 100% perpendicular polarization. In the remainder of this chapter, we will use selection rules appropriate to the static electronic polarizability, which is real and symmetric, so that only the A_g and H_g modes are first-order Raman active, as noted earlier.

The selection rules for the second-order sum and difference scattering arising from the second term in (23) within the harmonic approximation are a straightforward generalization: two modes f and f' cannot be second-order active unless their direct product representation $\boldsymbol{\Gamma}^f \times \boldsymbol{\Gamma}^{f'}$ includes irreducible representations contained in $(\boldsymbol{r} \times \boldsymbol{r})^s$. Thus for full icosahedral symmetry, $\boldsymbol{\Gamma}^f \times \boldsymbol{\Gamma}^{f'}$ must contain A_g and H_g. The resulting allowed second-order mode symmetry types are listed in Table 1.

For first-order IR and Raman activity, the net result for pure C_{60} is that there are very few active modes: the IR-active T_{1u} modes (four distinct frequencies), and the Raman-active A_g (two distinct frequencies) and H_g modes (eight distinct frequencies). To investigate the remaining $46-14 = 32$ distinct frequencies of the first-order "silent" IR and Raman modes, one can study the much more complicated second-order spectra or introduce perturbations that break the first-order selection rules. The latter approach will, of course, generally change the dynamics. In the case of C_{60}, however, isotopic substitutions and intermolecular interactions provide "gentle" perturbations which can nevertheless be probed by the sensitive first-order optical spectroscopies to yield information on the unperturbed silent modes [21,22].

1.3 Symmetry-Lowering Perturbations

The theoretical basis of Sect. 1.1 applies to both molecules and solids, provided that the Born-Oppenheimer approximation holds, whereas the symmetry considerations of Sect. 1.2 are for isolated molecules. This means that the calculated frequencies, eigenvectors, and spectroscopic intensities should be compared with experiments on isotopically pure molecules in the gas phase. However, all of the existing data on the vibrational properties of C_{60} stem from measurements carried out on thin films, crystals, and solutions. Fortunately, the forces between C_{60} molecules in the condensed phases are much weaker than the strong interatomic covalent forces within individual molecules. For instance, at room temperature solid C_{60} is a Van der Waals bound fcc lattice of approximately freely rotating molecules. The weakness of the intermolecular binding is further exemplified by the fact that the highest measured intermolecular phonon frequency at room temperature [23] is only ~ 50 cm^{-1}, well below that of the lowest intramolecular frequency, namely

272 cm^{-1} for the $H_g(1)$ "squashing" mode.[1] When the temperature is lowered below 260 K, the approximately free rotations are lost, but the intermolecular interactions and their effects on the dynamics remain relatively weak.

Another perturbation that is usually present in experiments on C_{60} arises from the naturally occurring distribution of carbon isotopes in the samples. Since the fractional mass change arising from the substitution of a single ^{12}C atom by a ^{13}C in a C_{60} molecule is 1/720, the dynamical effects induced by isotopic perturbations are also weak.

In the limit where the perturbations of the icosahedral symmetry are small and the associated changes of the dynamics can be neglected, the spectroscopic observation of silent modes provides direct information on the vibrational frequencies in icosahedral C_{60}, even if the precise form of the perturbation is not known. The intensity of the silent modes will of course be weak in this limit, but the high sensitivity of first-order techniques such as infrared absorption and Raman spectroscopy makes it possible to detect signals which are two or three orders of magnitude weaker than those arising from the strongest optically active modes. Additional information on the vibrational structure of the icosahedral molecule can be obtained when the perturbation is known in detail, allowing one to predict frequency shifts, selection rules, and spectroscopic intensities. Accordingly, we devote the remainder of this section to a discussion of isotopic and intermolecular interaction perturbations, which are not only well-characterized, but in practice are the most significant deviations from icosahedral symmetry. Not covered are extrinsic effects such as the presence of residual amounts of impurities, solvents, or other fullerenes, although the experimentalist must always keep these possibilities in mind. For example, it is known that even minute amounts of solvents can change the crystalline structure [24], and this is likely to affect the vibrational properties.

Isotopes

The simplest perturbation of the ideal icosahedral molecule arises from the presence of different carbon isotopes. The natural abundance of ^{13}C is 1.1%, with the result that 49% of the molecules obtained from natural graphite contain one or more ^{13}C isotopes. Studies of the isotopic distribution within the molecule show that it is truly random [25]. Excluding the unlikely possibility of significant zero-point effects, the mass perturbation does not affect the electronic structure of the molecule, so that force constants are unchanged. Hence calculations of the normal modes of icosahedral C_{60} can easily be extended to include the case of isotopic disorder, with no loss of accuracy. Details of such calculations are given in [21,22,26], and are summarized here in Sect. 2.5. These studies show that the analysis of the frequency shifts of modes which

[1] We are labeling the modes according to their frequencies. Thus the 8 distinct H_g mode frequencies will be listed as $H_g(1)$–$H_g(8)$, each of which is 5-fold degenerate.

are spectroscopically active for the unperturbed molecule provides information on silent modes. Furthermore, the invariance of the electronic structure under isotopic substitutions means that the IR and Raman intensities in isotopically disordered C_{60} can be computed using the same effective charges and electronic polarizability derivatives that are used for icosahedral C_{60}. For random isotopic disorder, all modes should become Raman and IR active, and their intensity can be predicted with accuracy.

Solid State Effects

The second form of commonly occurring symmetry lowering arises from the interactions between C_{60} molecules. This occurs not only in solid phases but also in solution, where C_{60} molecules have been shown to form aggregates [27]. The intermolecular interactions in crystalline C_{60} have been studied in much more detail, although a detailed analysis of the latest X-ray diffuse scattering experiments suggests that none of the models proposed so far is entirely satisfactory [28]. In order to understand the new spectroscopic features associated with the formation of C_{60} crystals, we must recast our discussion of the C_{60} vibrations using the standard theoretical framework for a periodic system. As mentioned above, the C_{60} molecules occupy fcc sites in the solid phase [29], and at room temperature, the rapid rotational diffusion of each molecule leads to an effective fcc crystal structure. At $T \approx 260$ K the crystal undergoes a phase transition, below which the four molecules in the conventional fcc cubic cell remain in the fcc sites but become orientationally inequivalent [23,24,30]. The orientational alignment occurs over a large temperature range, and the resulting low-temperature structure is simple cubic with four molecules per unit cell. The space group is P21/a (short $Pa\bar{3}$) [31].

In a lattice, the equilibrium site index ℓ of Sect. 1.1 is split: $\ell \rightarrow (\ell, b)$, where ℓ now labels the primitive unit cell of the Bravais lattice and the sites within each cell are labeled by the basis index b; thus for crystalline C_{60}, b ranges from 1 to $60s$, where s is the number of inequivalent molecules in each unit cell. The elements of the harmonic force constant matrix of (3) become $\Phi(\ell b\alpha, \ell' b'\alpha')$, and lattice periodicity renders them invariant to the addition of any cell index ℓ'' to both ℓ and ℓ'. Bloch's theorem then results in the normal modes being plane waves

$$\chi(\ell b\alpha|\vec{k}j) = \frac{e(b\alpha|\vec{k}j)}{\sqrt{N_c m_b}} \exp[i\vec{k} \cdot \vec{R}(\ell b)], \tag{27}$$

where $\vec{R}(\ell b)$ is the equilibrium position of site (ℓb), and periodic boundary conditions have been applied over a supercell containing N_c unit cells. The mode label f of Sect. 1.1 is now split into a wave vector $\vec{k}$ and polarization index j, with $j = 1, \ldots, 180s$. The $180s$-dimensional phonon polarization vectors $\boldsymbol{e}(\vec{k}j) \equiv \{e(b\alpha|\vec{k}j)\}$ are eigenvectors of the dynamical matrix, which

is given by the lattice Fourier transform of the force constant matrix:

$$D(b\alpha, b'\alpha'|\vec{k}) = \sum_{\ell'} \frac{\Phi(\ell b\alpha; \ell' b'\alpha')}{\sqrt{m_b m_{b'}}} \exp\{-i\vec{k}\cdot[\vec{R}(\ell b) - \vec{R}(\ell' b')]\}. \tag{28}$$

Finally, without loss of generality the periodic boundary condition supercell can be taken with an equal number L of primitive unit cells along each of the 3 Bravais lattice basis vectors, in which case $N_c = L^3$ and the allowed $\vec{k}$'s are given by $\vec{k} = \sum_{i=1}^{3} h_i \vec{b}_i / L_i$, where the three $\vec{b}_i$ are the basis vectors of the reciprocal lattice and the h_i's are positive or negative integers. The $\vec{k}$'s are restricted to the first Brillouin zone and total N_c in number.

In Sect. 1.2 we discussed the spectroscopic selection rules for molecular modes with index f. In the crystalline phase, periodicity imposes selection rules involving the wave vector $\vec{k}$. For either IR or Raman spectroscopy, wave vector conservation plus the fact that the photon wavelengths are essentially infinite on the scale of the intermolecular spacing, require that the sum of the wave vectors of the excited and/or destroyed modes must be zero. Thus for first-order absorption or scattering, only $\vec{k} = 0$ modes are active, while in second order one must have $\vec{k}_1 + \vec{k}_2 = 0$. Additional selection rules are obtained by considering the symmetry properties of the group of the wave vector associated with the phonons. For first-order spectroscopies, the group of $\vec{k} = 0$ is needed, and for solid C_{60} this is T_h, the point group of the lattice's space group. Second-order processes involve pairs of phonons with individual wave vectors away from $\vec{k} = 0$. Then the corresponding wave vector groups have lower symmetry, usually resulting in many more allowed combinations.

As noted, C_{60} forms a molecular solid for which the intermolecular interactions are much weaker than the intramolecular covalent forces. In such solids it is simple to track the evolution of the vibrational modes from isolated molecules to crystals. For C_{60}, the phonon dispersion relations $\omega(\vec{k}, j)$ decouple into a series of optic branches corresponding to the intramolecular vibrations above ~ 270 cm^{-1} and a second set of lower frequency branches which involve the molecules vibrating essentially as whole entities, i.e. as rigid balls, both translationally and rotationally (librations). The dispersion relations for the high frequency intramolecular optic branches reflect the weak ball-ball interactions and are therefore quite flat.

Well above T = 260 K, the orientational restoring forces between the balls can be neglected and there are no librational branches. Thus one can describe the low-frequency intermolecular modes to an excellent approximation as those of a simple monatomic fcc lattice of spherical "atoms," each with mass 12×60 amu, giving rise to three acoustic phonon branches.

In the low temperature simple cubic phase, the entire vibrational structure can be understood qualitatively by noting that the orientational forces which cause the phase transition are even weaker than the binding forces responsible for the average fcc structure. As a result, one can obtain a zero-order approximation to the vibrations in the low temperature phase by simply "folding"

the fcc Brillouin zone onto the smaller Brillouin zone of the simple cubic lattice with four molecules per unit cell. The weak reorientational potential induces small mode shifts and generally splits the degeneracies arising from the folding process. The folding of the three acoustic branches of the fcc lattice yields 12 low-frequency intermolecular phonon branches, of which 3 are acoustic and 9 are optical. In addition, the three rotational degrees of freedom of each molecule lead to 12 branches corresponding to librational motions. The highest observed librational frequency is of order 30 cm^{-1} [23]. This is lower than the highest translational frequency of 50 cm^{-1} and confirms the relative weakness of the reorientational potential. Finally, the folding of the 174 high-frequency fcc intramolecular optic branches derived from the modes of the isolated molecules yields 4×174 intramolecular optic branches, which are again relatively flat.

Table 3. Compatibility relations between the I_h C_{60} mode symmetries ($\omega \neq 0$) and the $\vec{k} = 0$ mode symmetries for the fcc standard-configuration lattice (space group $Fm\bar{3}$, point group T_h) and the simple cubic lattice (space group $Pa\bar{3}$, point group T_h, 4 molecules/cell). Modes belonging to A_g, E_g, and T_g are first-order Raman-active, whereas the T_u modes are first-order IR-active. Adapted from [11]

I_h	fcc ($Fm\bar{3}$)	I_h	sc ($Pa\bar{3}$)
A_g	A_g	$4A_g$	$A_g + T_g$
T_{1g}	T_g	$4T_{1g}$	$A_g + E_g + 3T_g$
T_{3g}	T_g	$4T_{3g}$	$A_g + E_g + 3T_g$
G_g	$A_g + T_g$	$4G_g$	$2A_g + E_g + 4T_g$
H_g	$E_g + T_g$	$4H_g$	$A_g + 2E_g + 5T_g$
A_u	A_u	$4A_u$	$A_u + T_u$
T_{1u}	T_u	$4T_{1u}$	$A_u + E_u + 3T_u$
T_{3u}	T_u	$4T_{3u}$	$A_u + E_u + 3T_u$
G_u	$A_u + T_u$	$4G_u$	$2A_u + E_u + 4T_u$
H_u	$E_u + T_u$	$4H_u$	$A_u + 2E_u + 5T_u$

Table 3 gives group-theoretic predicted splittings of the $\vec{k} = 0$ intramolecular modes in the solid phase. The first two columns give the splittings for a hypothetical ordered fcc structure in which the crystal's point symmetry about the origin of each molecule is T_h. This is achieved by orienting each C_{60} molecule with the 2-fold axes (which bisect the hexagon-hexagon bonds) parallel to the three orthogonal Cartesian axes. This is the so-called "standard structure" [32], and the space group is $Fm\bar{3}$. It should be noted that there are two equivalent standard structures, which are related by a reflection in the (110) planes. In real crystals, this leads to merohedral twinning and disorder, as will be discussed below. For T_h symmetry, modes belonging to the A_g, E_g, and T_g irreducible representations are first-order Raman-active, whereas the T_u modes are first-order IR-active. The third column in Table

3 is for reference and represents the situation for a hypothetical sc structure with four non-interacting I_h C_{60} molecules per unit cell. The last column gives the predicted splittings for the actual low temperature simple cubic phase, of space group $Pa\bar{3}$. In this structure, the four molecules in the simple cubic unit cell are again centered at fcc sites, but they are each rotated from their standard-structure orientation by the same angle, about different $\langle 111 \rangle$ axes. Although the point symmetry at each C_{60} site is then S_6, the presence of non-symmorphic operations (screw axes and glide planes) in $Pa\bar{3}$ results in the relevant point group for $\vec{k} = 0$ once again being T_h.[2] Hence the symmetry properties of this group still provide the spectroscopic selection rules for the first-order Raman- and IR-active phonons. Note from the second column of Table 3 that the formation of the hypothetical standard-structure fcc solid would split only the 4-fold and 5-fold degenerate modes of I_h C_{60}, whereas the last column shows that all of the levels are split by the reorientational potential in the low-temperature sc phase. Accordingly, one would generally expect the icosahedral A and T mode splittings, which arise only from the reorientational potential, to be smaller than the G and H mode splittings, which arise from both the formation of the solid and the reorientational potential.

A significant feature of the fully ordered crystal is that the T_h point group preserves the inversion symmetry, so that the first-order Raman and IR activities of the modes remain mutually exclusive, as for the ideal icosahedral molecule. This could be used to decide which symmetry-breaking mechanism is more important: if the isotopic perturbation dominates, it should be possible to observe the same silent modes in Raman and IR experiments. On the other hand, if the crystal field perturbation is stronger, one should see even-parity silent modes in Raman experiments and odd-parity silent modes in IR. Unfortunately, this comparison cannot be made easily because the weakness of the orientational forces prevents an ideal fully-ordered crystalline structure from being realized experimentally.

The most obvious deviation from an ordered crystalline structure occurs in the room temperature solid phase, where the molecules are rapidly changing their orientation. It was assumed originally that the C_{60} molecules were essentially free rotors about their lattice sites. This assumption was supported by a considerable amount of experimental data, including the excellent fit of

[2] For a mode at $\vec{k} = 0$, the displacement patterns are the same in each unit cell and are therefore invariant under any translation of the Bravais lattice. Hence the crystal symmetry operations relevant for $\vec{k} = 0$ modes are those involving no Bravais translations, namely pure point symmetry operations and nonsymmorphic operations consisting of point operations (rotation or reflection) followed by a fractional primitive cell translation (see [33]). These operations form a group which is isomorphic to one of the 32 crystallographic point groups, and for the space group $Pa\bar{3}$ this is T_h. Thus the group of the wave vector for the low temperature simple cubic phase of C_{60} is T_h, despite the fact that the highest site symmetry in this space group is S_6, occurring at each of the four C_{60} sites.

the X-ray diffraction pattern by assuming the molecule to be a spherical shell [24,30]. The effect of rotations on the spectroscopic activity of the molecule depends on whether the vibrations "see" an averaged external perturbation or a frozen configuration. In the first case, the observed spectra should be similar to those expected from C_{60} molecules in the gas phase. In the latter case, one should observe mode splittings and silent mode activation due to a virtually static random perturbation produced by the instantaneous orientation of the neighboring molecules. According to *Martin* et al. [34], the correct limit can be decided by comparing the lifetime (not the period) of the vibration relative to the rotational diffusion time. Applying this criterion to the T_{1u} modes, *Martin* et al. estimate an upper limit of 60 ps for their lifetime [34]. On the other hand, from the rotational diffusion constant measured with neutron scattering they estimate that a 60° rotation takes about 130 ps, so that it appears that crystalline C_{60} is closer to the frozen configuration limit [34]. More recent neutron scattering and X-ray data present a more complicated picture of the room temperature phase [23,35,36]. The data show non-negligible orientational correlations between neighboring molecules. The orientational distribution is found not to be isotropic. An excess atomic density of the order of 10% was found near the $\langle 110 \rangle$ directions, whereas a 16% deficit was found along the $\langle 111 \rangle$ directions [35]. This reflects a strong tendency for 5-fold axes to point along $\langle 110 \rangle$ directions. This orientation is nearly nine times more likely than the less favored orientation of the 5-fold axes along $\langle 111 \rangle$ directions [23]. The existence of these anisotropic orientations breaks the cubic and inversion symmetry and can lead to the activation of silent modes which are forbidden according to Table 3, even if the lifetime criterion discussed by *Martin* et al. [34] is not fulfilled.

We now discuss the low-temperature phase of solid C_{60} in more detail. As noted above, the effective high temperature fcc structure undergoes a phase transition at about 260 K, to the simple cubic $Pa\bar{3}$ phase, with four molecules per unit cell. In the fully-ordered version of this phase, the molecules remain centered at the fcc sites $\vec{t}_0 = (0,0,0)$, $\vec{t}_1 = (0,1/2,1/2)$, $\vec{t}_2 = (1/2,0,1/2)$, and $\vec{t}_3 = (1/2,1/2,0)$, but they have different orientations. This can be visualized by starting with the hypothetical fcc "standard structure" discussed above and rotating each molecule by the same angle Γ about a different $\langle 111 \rangle$ axis. The value of Γ is not determined by symmetry, but corresponds to an orientation for which an electron-rich double bond in one molecule faces an electron-poor pentagon face on its neighbor.

There are two sources of disorder in the $Pa\bar{3}$ crystal structure of C_{60} that limit the applicability of the $\vec{k} = 0$ mode splittings given in the last column of Table 3. The first type of disorder arises from the fact that there are eight distinct but equivalent $Pa\bar{3}$ structures, arising from the different choices for the four distinct $\langle 111 \rangle$ axes about which the molecules are rotated [31]. These eight structures can be conveniently described in terms of just one of the axis sets, as follows. Starting with the system in one of the two standard structures

and rotating each molecule by the same angle about the axes $\langle 111\rangle$, $\langle \bar{1}\bar{1}1\rangle$, $\langle \bar{1}1\bar{1}\rangle$, $\langle 1\bar{1}\bar{1}\rangle$, at positions (0,0,0), (1/2,0,1/2), (0,1/2,1/2), (1/2,1/2,0), respectively, yields a fully ordered $Pa\bar{3}$ structure. Then applying the translations $\vec{t}_1$, $\vec{t}_2$, and $\vec{t}_3$ yields three additional $Pa\bar{3}$ structures [32]. The same procedure applied to the other standard configuration then gives four additional $Pa\bar{3}$ structures. The eight total structures thus naturally divide into two sets, and each set gives a different contribution to the X-ray scattering intensity. The alternative structures coexist in real crystals in the form of macroscopic domains [37], yielding the so-called "merohedral twinning" [29,30]. The expression "merohedral disorder" has also been used in this context, but it is more properly applied to the case of alkali-metal fullerene intercalation compounds, where the two standard orientations become energy minima due to the alkali-metal–C_{60} interactions, and the molecules are randomly found in one of these two orientations [24]. The presence of merohedral twinning in crystalline C_{60} may scramble the polarization selection rules for Raman scattering, but is unlikely to activate silent modes other than those allowed by the fully ordered $Pa\bar{3}$ structure. This is because twinning does not destroy the local symmetry, and the interaction between distant C_{60} molecules across domain boundaries should be negligible. However, a second source of disorder in low-temperature C_{60} crystals does alter the local symmetry and may activate silent modes not allowed by the $Pa\bar{3}$ symmetry. The origin of this disorder is the existence of a secondary energy minimum for a rotation about a $\langle 111\rangle$ axis, which brings a double bond in one molecule close to a hexagonal face in a neighboring molecule (instead of a pentagonal face, as in the ground state) [23,24,30,38]. Below the phase transition at 260 K, the molecules librate about their equilibrium positions and occasionally jump between these two energy minima. At about 90 K the jumps are frozen on a laboratory time scale, and the crystal exhibits a residual disorder, whereby 84% of the molecules occupy the double-bond/pentagon configuration and the remaining 16% occupy the double-bond/hexagon configuration [38]. The existence of this disorder destroys the cubic and inversion symmetry and may activate all silent modes.

In summary, the symmetry of the ideal low-temperature crystalline C_{60} structure permits Raman scattering by all even parity molecular modes and infrared absorption by all odd parity molecular modes. Perturbations which destroy the inversion symmetry, such as the presence of isotopes or the existence of local orientational disorder due to the nearby energy minima can render all modes Raman and infrared active. Which of these mechanisms dominates can only be answered experimentally. The corresponding evidence is discussed in Sect. 2.

1.4 Survey of Theoretical Calculations

While spectroscopic work on C_{60} vibrations became possible only after the Krätschmer-Huffman breakthrough in 1990, theoretical studies began to ap-

pear as early as 1987 [39]. The success of the theoretical predictions can now be evaluated by comparing the calculated frequencies with experimentally determined values, as is done in Table 4. However, owing to the relatively small number (14) of frequencies which are directly accessible via the first-order optical spectroscopies, the comparison must be done with care. The frequency assignments in Table 4 will be discussed extensively in Sect. 2, where it will be shown that even with the addition of inelastic neutron scattering, second-order IR and Raman data, and fluorescence data, only 29 out of the total of 46 distinct vibrational frequencies are known with high certainty. This precludes a definitive evaluation of the accuracy of the different theoretical approaches. Another complication arises because, as pointed out in Sect. 1.2, each icosahedral irreducible representation except A_u appears more than once in the symmetry decomposition of the 174 vibrational modes. Comparisons between theory and experiment and among theoretical models themselves are usually made by simply ordering the modes according to their frequencies. However, a different match could be obtained by comparing eigenvectors. For example, the $G_u(2)$ and $G_u(3)$ modes of Table 4 are quite close in frequency, and the eigenvector of the lower frequency mode – which the experimentalist would call $G_u(2)$ – might actually be closer to the eigenvector of the G_u mode with the theoretically predicted higher frequency, which would be called $G_u(3)$ by the theorist. Unfortunately, the sheer amount of data necessary to specify each of the 180-dimensional C_{60} mode eigenvectors, their nonuniqueness with respect to mode degeneracies, and the difficulty of obtaining them experimentally have precluded eigenvector comparisons. As far as we know, the only direct experimental studies of C_{60} mode eigenvectors is the recent neutron scattering work of *Heid* and coworkers [40].

Table 4. Recommended values (in cm^{-1}) for the 46 distinct normal mode frequencies of an isolated C_{60} molecule. The symmetry types of the ten first-order Raman and four first-order infrared active modes are labeled with bold-face characters in the first column. Bold type is also used in the second column for the frequencies of modes which have been clearly identified on the basis of spectroscopic selection rules or inelastic neutron scattering data. Whenever possible, low-temperature experimental values were used. The third and fourth columns give representative first-principles LDA-based theoretical results, together with their percent errors, as discussed in the text

Mode	Frequency	Theoretical Calculations	
		Giannozzi and *Baroni* [47]	*Adams* et al.[53]
$\mathbf{H_g(1)}$	**272**	259 (-4.8%)	259 (-4.8%)
$T_{3u}(1)$	**342**	337 (-1.5%)	330 (-3.5%)
$G_u(1)$	**353**	349 (-1.1%)	353 (0.0%)

continued on following page

continued from previous page

$H_u(1)$	**403**	399 (-1.0%)	399 (-1.0%)
$H_g(2)$	**433**	425 (-1.8%)	427 (-1.4%)
$G_g(1)$	**485**	480 (-1.0%)	484 (-0.2%)
$A_g(1)$	**496**	495 (-0.2%)	494 (-0.4%)
$T_{1u}(1)$	**526**	527 (0.2%)	522 (-0.8%)
$H_u(2)$	**534**	530 (-0.7%)	533 (-0.2%)
$T_{3g}(1)$	**553**	548 (-0.9%)	547 (-1.1%)
$G_g(2)$	**567**	566 (-0.2%)	554 (-2.3%)
$T_{1g}(1)$	**568**	564 (-0.7%)	565 (-0.5%)
$T_{1u}(2)$	**575**	586 (1.9%)	570 (-0.9%)
$H_u(3)$	**668**	662 (-0.9%)	654 (-2.1%)
$H_g(3)$	**709**	711 (0.3%)	694 (-2.1%)
$G_g(3)$	**736**	762 (3.5%)	745 (1.2%)
$H_u(4)$	**743**	741 (-0.3%)	727 (-2.2%)
$T_{3u}(2)$	753	716 (-4.9%)	696 (-7.6%)
$T_{3g}(2)$	756	767 (1.5%)	717 (-5.2%)
$G_u(2)$	764	748 (-2.1%)	708 (-7.3%)
$H_g(4)$	**772**	783 (1.4%)	760 (-1.6%)
$G_u(3)$	776	782 (0.8%)	753 (-3.0%)
$T_{3g}(3)$	796	794 (-0.3%)	757 (-4.9%)
$T_{1g}(2)$	831	823 (-1.0%)	813 (-2.2%)
$G_u(4)$	961	975 (1.5%)	970 (0.9%)
$T_{3u}(3)$	973	993 (2.1%)	954 (-2.0%)
A_u	984	943 (-4.2%)	929 (-5.6%)
$G_g(4)$	1079	1118 (3.6%)	1123 (4.1%)
$H_g(5)$	**1099**	1120 (1.9%)	1103 (0.4%)
$T_{1u}(3)$	**1182**	1218 (3.0%)	1227 (3.8%)
$T_{3u}(4)$	1205	1228 (1.9%)	1239 (2.8%)
$H_u(5)$	**1223**	1231 (0.7%)	1243 (1.6%)
$H_g(6)$	**1252**	1281 (2.3%)	1328 (6.1%)
$T_{1g}(3)$	1289	1296 (0.5%)	1309 (1.6%)
$G_u(5)$	**1309**	1334 (1.9%)	1369 (4.6%)
$G_g(5)$	1310	1322 (0.9%)	1332 (1.7%)
$H_u(6)$	1344	1363 (1.4%)	1387 (3.2%)
$T_{3g}(4)$	1345	1363 (1.3%)	1385 (3.0%)
$G_u(6)$	**1422**	1452 (2.1%)	1525 (7.2%)
$H_g(7)$	**1425**	1450 (1.8%)	1535 (7.7%)
$T_{1u}(4)$	**1429**	1462 (2.3%)	1560 (9.2%)

continued on following page

continued from previous page

$A_g(2)$	**1470**	1504 (2.3%)	1607 (9.3%)
$G_g(6)$	1482	1512 (2.0%)	1578 (6.5%)
$T_{3u}(5)$	1525	1535 (0.7%)	1598 (4.8%)
$H_u(7)$	**1567**	1569 (0.1%)	1622 (3.5%)
$H_g(8)$	**1575**	1578 (0.2%)	1628 (3.4%)

Conceptually, perhaps the simplest vibrational model applied to C_{60} results from a continuum approximation in which the molecule is treated as a thin elastic spherical shell. While the predictive accuracy of such a model may not be sufficient for spectroscopic assignments, the vibrational analysis of a spherical shell can contribute to the qualitative understanding of the molecular modes, particularly those with lower frequencies. A case in point is the near degeneracy of the $T_{3u}(1)$ and $G_u(1)$ modes of C_{60}. This quasi degeneracy is not accidental if one considers these modes to originate from the 7-fold degenerate $\ell = 3$ multiplet of the O(3) group. This multiplet is split by the icosahedral perturbation, and the smallness of the observed splitting suggests that a continuum model might be a useful approximation for the lowest-energy modes of C_{60}. However, in spite of its conceptual simplicity, the problem of an elastic spherical shell is rather complicated analytically, and the two published papers following this idea disagree in their detailed predictions [41,42].

Prior to 1990, normal mode calculations treating the C_{60} molecule as a discrete system used force constants transferred from other molecules containing carbon-carbon bonds, such as benzene [16], or relied on semi-empirical quantum chemistry calculations (e.g. MNDO, AM1, or QCFF/PI [39,43–45]). Within these early calculations, the best agreement for the 29 highlighted frequencies in Table 4 holds for the QCFF/PI calculations of *Negri* et al. [45], with an average deviation from experiment of 5.7%.

First principles calculations based on density functional theory within the local density approximation (LDA) began to appear after 1990. Such calculations give the best agreement with the known C_{60} vibrational frequencies, with an average deviation ranging from 1.8% to 3.9%. One of the main differences between the various implementations of the LDA approach stems from the type of basis functions used for the electronic states. Expansions in orthogonal plane waves are advantageous in that the convergence of a calculation can be improved by simply adding more plane waves. Moreover, this basis lends itself to the derivation of convenient perturbative expressions for the dynamical matrix of (28). This Density Functional Perturbation Theory approach [46] was used by *Giannozzi* and *Baroni* [47] to compute the vibrational frequencies of C_{60}, with an average deviation from experiment of only 1.8%. These frequencies are given in the second column of Table 4. Another well-known plane-wave implementation of LDA techniques is that of *Car* and *Parrinello* [48], which uses atomic forces computed directly from

the electronic states to perform molecular dynamics calculations. An early application of this method to the dynamics of C_{60} is given in [49]. A plane wave basis necessitates the use of periodic boundary conditions, and for isolated molecules the associated supercell is simply taken to be much larger than the molecule.

Since plane waves are not particularly well-suited for describing compact atomic orbitals such as those in fullerenes, plane wave expansions can become computationally very intensive (24000 plane waves were used for the molecular C_{60} calculations of [47]). The use of a small number of localized basis functions is a natural choice for such systems. Several methods of this type have been applied to the molecular properties of C_{60} [50–52]. The agreement with experiment is excellent. *Quong* et al. [51] and *Wang* et al. [52] used different all-electron localized basis sets within the LDA and obtained average deviations from the experimental frequencies of 1.9% and 2.2%, respectively, very close to the results of *Giannozzi* and *Baroni* [47]. In 1991, *Adams* et al. [50] used a local pseudoatomic orbital minimal sp^3 basis for each atom and obtained an average deviation from experiment of $\approx 10\%$. Subsequent refinements [53] have improved this to 3.9%. The general method they employed was developed by *Sankey* et al. [54] and utilizes approximations which render it computationally very efficient, giving it the significant advantage of being suitable for much larger fullerenes, including tubes and capsules [55] as well as polymerized fullerenes [53]. Because this method underlies some of our subsequent discussion, we have included its predicted frequencies in Table 4 and will now briefly highlight a few of its key points.

First, the local orbitals are computed from a self-consistent LDA pseudopotential calculation for the free atom, but subject to the boundary condition that the wave functions vanish at a finite cutoff radius r_c, which for fullerenes is taken at 4.1 Bohr radii[3] This has the effect of slightly exciting the orbitals from their ground states, crudely representing the effects of electronic confinement in the molecule. More important from a computational standpoint is the fact that this vastly decreases the number of electronic overlap integrations that must be performed. Second, the Kohn-Sham self-consistent energy functional is replaced by the much simpler non self-consistent *Harris* energy functional [56], which takes the input charge density to be a sum of the neutral atom densities. The elimination of the need to compute the electronic charge density self-consistently, together with the finite orbital confinement, results in a computationally very efficient method to

[3] Note that this value $r_c = 4.1$ Bohr radii differs from the original value (3.3 Bohr radii) used in [50]. As is detailed in the first and third publications cited in [53], the use of 4.1, together with a minor alteration in the calculation of the so-called electron double-counting correction, substantially improves the results of [50]. The measured bond lengths of C_{60} are reproduced, and the average deviation of the calculated frequencies of the 14 first-order infrared and Raman active modes is 3.7%, compared with $\approx 10\%$ in [50].

obtain the atomic potential energy function $V(\boldsymbol{u}) = E_0(\boldsymbol{u})$ of Sect. 1.1 for an arbitrary atomic configuration. Moreover, methods based on the Hellmann-Feynman theorem can be used for accurate calculations of the corresponding atomic forces $F(\ell\alpha) = -\partial V(\boldsymbol{u})/\partial u(\ell\alpha)$ directly from the electronic states [57], avoiding the necessity of numerically differentiating V. One can then either obtain the harmonic force constant matrix as discussed below or perform molecular dynamics simulations of real-time atomic motions, as in the Car-Parrinello method. The net result is a computationally fast and entirely real-space scheme to calculate the electronic structure, dynamics, and equilibrium geometry. No *a priori* symmetrization of the electronic states is made. For C_{60}, the calculations reproduce the experimental bond lengths, and yield all of the mode frequencies with an average deviation of 3.9%, as noted above.

In computing the dynamics of C_{60} from first-principles, the high symmetry of the molecule greatly simplifies the work. A given row (or column) of the harmonic force constant matrix can be obtained simply by displacing one of the atoms and computing the resulting force per unit displacement on each atom. Specifically, if the atom at ℓ' is given a displacement $u(\ell'\alpha')$ in the direction α' and the remaining atoms are fixed at their equilibrium positions, (3) gives $\Phi(\ell\alpha, \ell'\alpha') = -F(\ell\alpha)/u(\ell'\alpha')$. Since all of the equilibrium sites of C_{60} are symmetrically equivalent only one atom must be displaced, and the remaining elements of the force constant matrix can be obtained by applying point symmetry operations. This method was employed in the local orbitals first-principles calculations of [51–53]. For example, the frequencies given in the fourth column of Table 4 were obtained by first displacing a single atom by 0.0125 Å along $\pm x, \pm y, \pm z$. For each of the six configurations, the force (per unit displacement) was computed at each site, and the results for plus and minus dispacements were averaged to eliminate cubic and higher odd-order anharmonicity, after which the remaining force constants were generated by applying icosahedral symmetry operations. The resulting 180×180 force constant matrix was then diagonalized, and the mode symmetry types were determined by applying group theoretic projection operators to the eigenvectors. Analogous simplifications, based on the high symmetry of C_{60}, have been used in the Density Functional Perturbation Theory plane-wave calculations of [47]. A different approach is to employ projection operators from the outset, to obtain vibrational symmetry coordinates [50]; however, this method involves computing the first-principles forces for many more configurations. Within some of the first-principles methods, it is also possible to completely bypass the computation of the force constant matrix by using the first-principles forces in molecular dynamics and performing a Fourier transform of the resulting time-dependent displacements. This approach was followed by *Adams* et al. [50], and also by *Feuston* et al. [58] using Car-Parrinello molecular dynamics. Although much more demanding computationally, since the full LDA electronic structure calculation must be carried

out at each time step, this method has the advantage that it is not restricted to small displacements, so that anharmonic dynamics can be explored.

While the overall accuracy of first-principles calculations is impressive, it remains between one and two orders of magnitude less than the experimental accuracy. The residual theoretical uncertainty of 1–3% renders it difficult to predict effects which are sensitive to the occurrence of modes with frequency separations of this magnitude. An example is the isotope-induced change of the $A_g(2)$ pentagonal pinch mode Raman peak in molecular C_{60}, which is sensitive to the location of nearby unperturbed frequencies, as detailed in [22] and summarized in Sect. 2.4.

Once experimental vibrational frequencies became available, several empirical models were introduced. The force constants in these models are obtained from fits to the Raman-active and infrared-active modes. The resulting frequencies, however, are in no better agreement with experiment than those obtained from first-principles methods. *Jishi* et al. [59] used an eight-parameter model fit to the ten Raman frequencies of C_{60}. *Feldman* et al. [60] used a seven-parameter model fit to the frequencies of the 14 first-order infrared and Raman active modes of C_{60}. The adiabatic bond charge model, which is successful in reproducing the vibrational properties of tetrahedral semiconductors [61], has also been applied to fullerenes [62,63]. The average discrepancy with experiment obtained from these calculations is about 5%. If one considers the fact that the comparison with experiment includes the modes that are being fit, its is apparent that empirical methods are significantly worse than first-principles approaches. The reasons for this become clear when one examines the spatial range of the interatomic forces in C_{60}. Jishi et al. were the first to note that a model which includes only nearest-neighbor interactions cannot account for the frequencies of the two A_g modes. Hence their model includes up to third-neighbor force constants. However, a careful analysis by *Quong* et al. [51] of their first-principles results shows that interatomic force constants extend much further than this – interactions up to seven neighbors must be included to guarantee convergence of the eigenvalues to within 5 cm^{-1}. Similar conclusions regarding the range of the interatomic interactions in C_{60} can be drawn from the work of *Bohnen* et al. [64].

Several theoretical studies have appeared on the intermolecular potential that determines the "external," e.g. phonon modes in crystalline C_{60}. While some of these studies concentrate on the prediction of the stable crystalline structures and phase transitions, a few give phonon calculations [65,66]. The intermolecular potential is usually modeled as a combination of Morse, van der Waals and Coulomb potentials. First-principles calculations of the intermolecular potential have appeared only recently [67], and they have not yet been applied to the phonon modes.

2 Vibrational Spectroscopy of C_{60} Molecules

A basic goal of vibrational studies of C_{60} is the identification of its 46 distinct mode frequencies. The discussion of Sect. 1.2 showed that for perfectly icosahedral C_{60} only 14 of these frequencies can be determined using first-order IR absorption and Raman scattering. In Sect. 1.3 we suggested that information about the 32 silent modes can be obtained by exploiting deviations from icosahedral symmetry, or by performing second-order Raman scattering and infrared absorption experiments. In addition, a number of other techniques, including inelastic neutron scattering, fluorescence spectroscopy and high-resolution electron energy-loss spectroscopy, provide information about silent modes. Unfortunately, none of these methods – considered individually – yields an unambiguous mode identification. In this section we discuss our best attempt at assigning vibrational frequencies on the basis of all the experimental evidence available. We first summarize our conclusions in Sect. 2.1, and then focus on the contributions from different techniques in Sects. 2.2–2.8. For completeness, Sect. 2.9 briefly discusses some alternative assignments that are found in the literature.

2.1 The Assignment of Active and Silent Modes

Table 4 on page 19 gives our recommended values for the 46 different vibrational frequencies in C_{60}, together with two sets of first principles predictions [47,53]. Also shown in parentheses are the discrepancies between the calculated and recommended values. The frequencies of the modes that in our opinion have been clearly identified appear in bold type. For the remaining modes the uncertainty in the assignments varies, and future work may lead to somewhat different assignments. Note that the set of well-identified frequencies includes not only the first-order active IR and Raman modes, but also a significant number of silent modes. Whenever possible, the experimental frequencies were selected from low-temperature data. However, since the data originate from different sources, relative errors of the order of 2 cm^{-1} are unavoidable. In particular, the widespread use of array detectors for Raman spectroscopy leads to discrepancies of the order of 2 cm^{-1} between different sets of data in the literature, probably as a result of small differences in the detector calibrations.

Several alternative assignments of vibrational frequencies in C_{60} can be found in the literature [68–76]. *Martin* et al. [70] combined their own high-resolution first- and second-order IR data with published Raman measurements [68] and neutron scattering results [77] to arrive at a complete set of frequencies. Some of the frequencies proposed in [70] agree with those in Table 4. Others, however, differ from the theoretical predictions given there by as much as 70%. These large discrepancies seem unlikely in view of the remarkable accuracy (better than 5%) of state-of-the-art first-principles methods. In fact, the requirement of consistency with theory can be a powerful tool

for the assignment of mode frequencies. This was recognized by *Dong* et al. [68] and *Wang* et al. [69], who used an empirical model to calculate the mode frequencies. Their frequencies were then adjusted so that the fine structure observed in the Raman and IR spectra of C_{60} could be explained in terms of second-order overtones and combinations. The resulting frequency assignments [69] are closer to ours (Table 4), but some silent mode frequencies differ by as much as 20%. This discrepancy is understandable if one recalls that empirical vibrational models do not treat active and silent modes on an equal footing. Instead, the known frequencies of the active modes are used as input parameters to generate the interatomic potentials. This makes it difficult to assess the accuracy of the silent mode frequencies predicted by these models. In contrast, for first-principles methods there is no *a priori* reason why the silent mode frequencies should be less accurate than those of the active modes. Since the agreement between theoretical predictions and active mode frequencies turns out to be better than 5%, silent mode frequency assignments which differ from the first-principles predictions by much more than 5% are questionable.

Assignments of silent mode frequencies which are consistent with the Density Functional Perturbation Theory calculations of *Giannozzi* and *Baroni* [47] were published by *Schettino* et al. [72] and by *Menéndez* and *Guha* [71]. The latter authors observed that the error in the predicted active mode frequencies has a relatively smooth frequency dependence. The calculations underestimate the low frequencies, while overestimating the high frequencies, as can be seen in Table 4. By making the *ad hoc* assumption that the "error curve" for the active modes also applies to the silent modes, *Menéndez* and *Guha* [71] generated a set of "adjusted first-principles" frequencies which they used as the starting point for their assignments. The agreement between the assigned frequencies and the adjusted first-principles values is quite remarkable, with a standard deviation of only 2 cm^{-1}. Subsequent neutron scattering experiments [40,78], have confirmed all of the assignments of [71] for frequencies below 700 cm^{-1}. The recommended frequencies for several of the modes above 700 cm^{-1} in Table 4 are somewhat different from those of [71]. The revised frequencies given here are in better agreement with the latest inelastic neutron scattering experiments [40,78,79], as well as with recent optical emission experiments [80].

2.2 First-Order Infrared Absorption and Raman Scattering Experiments

Shortly after the discovery of a method to produce C_{60} in macroscopic quantities [2], the observation of four strong infrared absorption peaks provided strong evidence for the proposed icosahedral structure of the molecule [81]. With regard to Raman scattering, the unequivocal observation of the ten first-order peaks allowed by group theory required additional advances in the extraction of C_{60} from the fullerene soot. This was because some of the

first-order Raman peaks of C_{60} are very weak and could be confused with weak lines arising from C_{70} or other contaminants. Only after chromatographically separated fullerenes became available was it possible to obtain unambiguous evidence for the consistency of the Raman spectrum with the icosahedral symmetry of C_{60} [82,83]. Figures 1 and 2 show infrared absorption and Raman scattering spectra from C_{60} films [84]. The measured values of the first-order IR and Raman frequencies are given in Table 4.

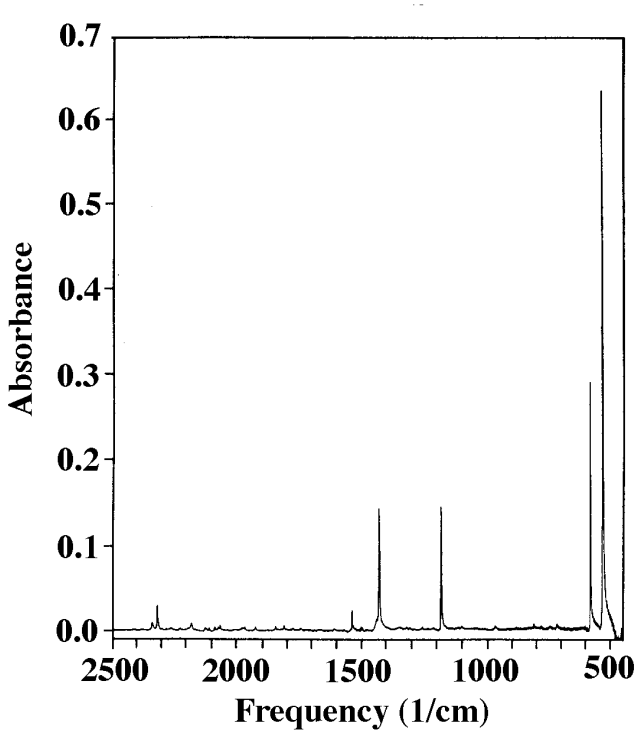

Fig. 1. Fourier transform IR spectra of a 1.4 mm thick film of C_{60}. After *Chase* et al. [84]

2.3 Second-Order Infrared Absorption and Raman Scattering Experiments

Infrared absorption and Raman scattering involving two vibrational quanta play a key role for the mode frequency assignments. This is because, as discussed in Sect. 1.2, the corresponding selection rules are significantly less restrictive than for first-order absorption or scattering. Table 1 listed these

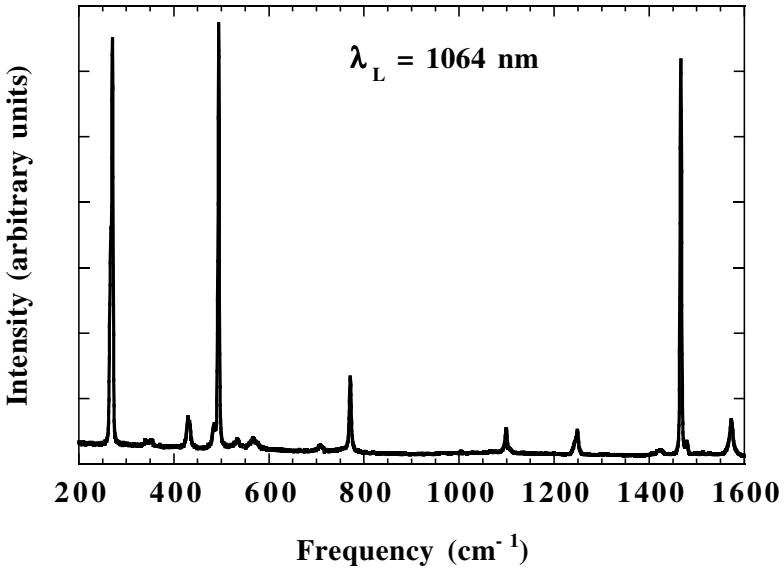

Fig. 2. Room temperature Fourier transform Raman spectrum of a C_{60} film. The laser excitation wavelength is 1064 nm. After *Chase* et al. [84]

selection rules for molecular C_{60}, and it is seen that all of the vibrational symmetries can participate in second order processes. For summation processes, this leads to the possibility of a total of 511 different second-order Raman peak frequencies and 380 different second-order IR frequencies. Notice from Table 1 that the inversion symmetry of the molecule imposes the restriction that in Raman summation processes, the two modes must be both even or both odd, whereas in IR they must have opposite parity.

Second-order Raman scattering in C_{60} was reported as early as 1991 [85]. A systematic study of all peaks between 250 cm^{-1} and 3400 cm^{-1} was given by *Dong* et al. [68]. In addition to the 10 first-order Raman peaks of C_{60}, these authors identified 90 additional weaker peaks between 343 cm^{-1} and 3385 cm^{-1}. Several other groups also studied the fine structure in the C_{60} Raman spectrum [73,86–89]. For the second-order IR spectrum of C_{60}, systematic studies were carried out by *Martin* et al. [70], *Wang* et al. [52], and *Bowmar* et al. [73]. The data of Martin et al. were taken at 77 K, whereas the other two sets correspond to room temperature. The agreement between the three sets is good, and that between Martin et al. and Wang et al. is excellent.

Despite the fact that fine structure in IR and Raman spectra provides a powerful tool for the assignment of silent mode frequencies, a failure to explain a few peaks as second-order processes cannot be used to rule out a particular frequency assignment. This is because an observed peak could be either a third-order (or higher) combination or a silent mode which becomes weakly active due to an external perturbation. Both possibilities are known

to occur. Table 4 indicates that the highest energy vibration in C_{60} is the $H_g(8)$ mode at 1575 cm^{-1}, implying that the highest possible frequency for a second-order peak is 3150 cm^{-1}. However, Raman and IR peaks well above this frequency are observed experimentally [52,68,70], so that they must be due to higher-order processes. Since there is no reason for such processes to be limited to frequencies above the second-order cutoff at 3150 cm^{-1}, the possibility of their occurrence has to be kept in mind when analyzing all of the fine structure in the Raman and IR spectra. Similarly, the lowest vibrational frequency in the C_{60} molecule is the $H_g(1)$ mode at 272 cm^{-1}, setting a lower limit of 544 cm^{-1} for peaks which can be assigned to second-order spectra (provided that difference processes can be neglected, as is the case at low temperatures). Nevertheless, extra Raman and IR peaks have been observed below 544 cm^{-1} in experiments performed at the lowest temperatures [68,70], and they must be ascribed to weakly allowed first-order processes. Possible mechanisms are discussed in Sects. 1.2 and 2.4. Again, there is no *a priori* reason why the observation of "forbidden" fundamentals should be limited to modes below 544 cm^{-1}. Therefore the possibility of such processes above this frequency should also be kept in mind.

As a result of the different alternative explanations and the observation of fewer peaks than allowed by group theory, the interpretation of second-order spectra is hardly unique. From the 90 additional Raman peaks identified by *Dong* et al. [68], 86 have frequencies equal to or less than 3150 cm^{-1}. A total of 83 such peaks can be explained as allowed second-order combinations or as forbidden first-order processes (i.e. first-order Raman scattering by silent modes), using the assignments of Table 4. The standard deviation between the frequencies so computed and the experimental frequencies is only 0.3 cm^{-1}. Three peaks observed by *Dong* et al. [68], at 2463 cm^{-1}, 2782 cm^{-1}, and 3118 cm^{-1}, cannot be assigned to second-order processes on the basis of the mode frequencies in Table 4. These observed peaks are at least one order of magnitude weaker than the strongest second-order lines – which typically involve combinations of H_g modes – and they have not been reported by other groups. All three of these peaks can be interpreted as third-order combinations involving H_g modes, so that their observation cannot be used to rule out the assignments of Table 4.

We have also verified that a total of 97 extra infrared absorption peaks observed by *Martin* et al. [70] and *Wang* et al. [52] can be explained either as second-order combinations or as forbidden fundamentals, using the mode frequency assignments in Table 4. The standard deviation of 0.3 cm^{-1} is the same as for the Raman fine structure.

2.4 Isotopic and Crystalline Perturbations: Spectroscopic Evidence

The spectroscopic activation of silent modes by isotopic and crystal field perturbations provides an important tool for the study of the vibrational

properties of C_{60}. The discussion in Sect. 1.3 shows that the two perturbations behave quite differently: isotopes remove the inversion symmetry, thus allowing modes to be both Raman and infrared active in first order. On the other hand, the inversion operator is an element of T_h, so that as long as the T_h symmetry of $\vec{k} = 0$ is preserved, only even modes will be observable with first-order Raman spectroscopy and only odd modes will be first-order IR active. High resolution IR and Raman experiments show peaks at most of the silent mode fundamental frequencies in Table 4. On the basis of this table, however, allowed second-order combinations can be predicted to occur near many of these frequencies. Therefore, only those extra peaks observed at the low end of the spectrum, where no second-order combinations are possible, can be ascribed with certainty to silent modes. In experiments on solid C_{60} films at low temperatures, *Dong* et al. [68] reported Raman peaks at all of the mode frequencies below 500 cm^{-1} in Table 4. Peaks at the same frequencies (with the exception of the frequencies of the $H_g(1)$ and $A_g(1)$ modes) were also observed in IR experiments on similar films by *Martin* et al. [70]. This indicates that Raman and IR experiments do not discriminate strongly between even-parity and odd-parity silent modes, suggesting that the isotopic perturbation might be the most important symmetry breaking mechanism. However, systematic investigations of the isotope effect have failed to show any strong correlation between isotopic impurity concentrations and the Raman or IR intensities of silent modes [34,89].

The lack of correlation between the intensity of Raman and IR peaks assigned to silent modes and the concentration of ^{13}C isotopes is consistent with our calculations of these intensities using the methods described in Sects. 3 and 4 [90]. These calculations show that isotopes play a very minor role in activating silent modes, so that their observation must primarily be due to crystal field effects. Disorder that reduces the $\vec{k} = 0$ symmetry from T_h, as discussed in Sect. 1.3, must play an important role, since it provides the only possible explanation for the removal of the inversion symmetry revealed by the experiments. Nevertheless, one might expect those silent modes which become allowed under T_h to give stronger signals than those which are allowed only due to disorder in the crystalline phases. While a systematic investigation is lacking, some experimental evidence supports this idea. For example, Raman peaks which according to Table 4 correspond to G_g modes systematically appear in Raman spectra reported by several different authors [68,84,86,87,89]. As shown in Table 3 for the fcc ($Fm\bar{3}$) structure, G_g modes are unique in that they belong to the only icosahedral irreducible representation (other than A_g) which contains the identity representation in the decomposition products under T_h symmetry.

Our discussion so far has concentrated on the activation of silent modes by perturbations which lower the icosahedral symmetry. Information about these perturbations can also be obtained by studying their effect on spectroscopically active modes. In fact, it became clear from the earliest Raman

studies of C_{60} that the depolarization ratio for H_g modes falls systematically below the value 0.75 predicted on the basis of icosahedral symmetry. The observed depolarization ratio for the two A_g modes is much closer to the predicted value of zero. No detailed explanation has been provided. *Snoke* and *Cardona* [91] argued that whereas a general perturbation ϵ can change the depolarization ratio for H_g modes by an amount proportional to ϵ, the change for A_g modes must necessarily be at least quadratic in ϵ, since the unperturbed predicted value of zero is the lowest possible for a depolarization ratio.

The discontinuous temperature dependence of the Raman and IR mode frequencies near the ordering phase transition, together with the splitting of these modes at low temperatures, are strong manifestations of crystal field effects on the intramolecular vibrations of C_{60} [92–96]. In most cases, however, these splittings are not well understood. Part of the difficulties stem from the comparable size of the splittings induced by isotopic and crystal-field perturbations, which dictate the need for isotopically pure samples in order to investigate crystal field effects. Perhaps more serious is the possibility of accidental degeneracies between active and silent modes. For closely spaced modes, any small perturbation may induce substantial mixing, so that the analysis of crystal field splittings of active modes requires knowledge of the frequency of all nearby modes. A good example of these complications is provided by the crystal field splittings of the T_{1u} modes. High resolution infrared reflectance experiment by *Homes* et al. [94] revealed a complicated splitting pattern for all T_{1u} modes except $T_{1u}(2)$. This pattern was found to be strikingly different in isotopically pure samples [95]. The analysis of the splittings was based on the assumption that no silent modes have a frequency close to any of the T_{1u} modes. Our assignments in Table 4, however, indicate the presence of silent modes very close in frequency to $T_{1u}(1)$, $T_{1u}(2)$ and $T_{1u}(4)$, a fact that may require a new interpretation of some of the observed splittings.

A more direct way of studying crystal field effects is to perform spectroscopic studies of those external lattice modes which are due exclusively to the weak intermolecular potential. The external modes of the C_{60} crystal have frequencies below 60 cm^{-1}, which makes them difficult to observe. However, an accurate mapping of the phonon dispersion relations has been obtained with inelastic neutron scattering [23,97]. The zone-center modes are expected to be optically active and have the convenient feature that those which correspond to translational vibrations are IR active and those which correspond to librational motions are Raman active [11]. Both types of modes have been observed [98–100], and their frequencies are consistent with the neutron scattering experiments.

2.5 Quantitative Assessment of Isotope Effects

In previous work [21,22,26], we showed that detailed experimental/theoretical studies of isotopic perturbations on the Raman active modes of C_{60} provide a sensitive probe of the nearby silent modes. Here we summarize aspects of that work, incorporating our present mode assignment of Table 4.

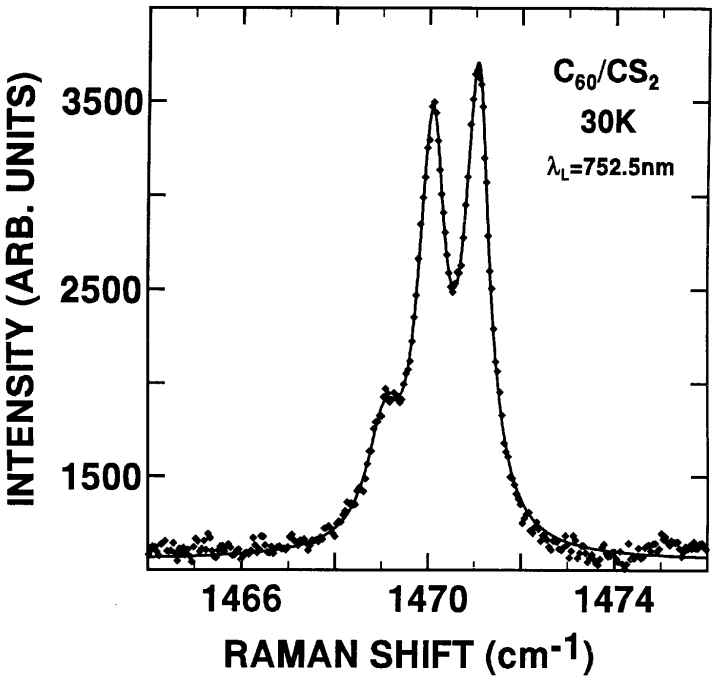

Fig. 3. Unpolarized Raman spectrum in the frequency region of the pentagonal pinch mode, for a frozen sample of non-isotopically enriched C_{60} in CS_2 at 30 K. The points represent the experimental data, while the solid curve is a 3-Lorentzian fit. The highest-frequency peak is assigned to the totally-symmetric pentagonal-pinch $A_g(2)$ mode in isotopically pure $^{12}C_{60}$. The other two peaks are assigned to the perturbed pentagonal-pinch mode in molecules having one and two ^{13}C isotopes, respectively. After *Guha* et al. [22]

Specifically, we analyzed the effects of ^{13}C isotopes on high-resolution Raman spectra in the vicinity of the intense first-order $A_g(2)$ peak that occurs

at 1471 cm^{-1} in the isotopically pure icosahedral molecule.[4] This is the familiar "pentagonal pinch" mode, in which the atoms vibrate almost purely tangentially, towards or away from the centers of the 12 pentagons. With isotopes present, the molecule's adiabatic electronic states are unchanged (we are neglecting small zero-point effects), leaving the force-constant matrix, the IR effective charges, and the Raman polarizabilities unaffected. However, the lowered symmetry introduced by mass perturbations relaxes the spectroscopic selection rules and allows the unperturbed modes to couple. Since the perturbation introduced by each ^{13}C isotope in C_{60} is only of order 1/720, the effects on the dynamics are indeed weak, although readily observable in Raman or IR.

The 1.1% natural abundance of ^{13}C means that a C_{60} molecule has a 49% probability of containing one or more of these isotopes. Figure 3 shows our high-resolution spectrum for a sample having the natural isotopic abundance. The C_{60} was dissolved in CS_2, and the spectrum was measured at T =30 K. The solid curve is a 3-Lorentzian fit to the experimental points. As detailed in [21,22,26], we attribute the three clearly-resolved peaks to scattering from molecules containing 0, 1, or 2 ^{13}C atoms, respectively. The measured separation between the first and second peaks is 0.98 ± 0.01 cm^{-1}, while for the second and third peaks, it is 1.02 ± 0.02 cm^{-1}. As shown below, these splittings are predicted essentially exactly by first-order nondegenerate perturbation theory.

The bottom panel of Fig. 4 shows the analogous spectrum, but for an isotopically enriched sample. The top panel gives the measured isotopic mass distribution for this sample. It is apparent that the two lineshapes show a remarkable correlation. Again, a very simple perturbation-theoretic argument will be seen to explain this result, while deeper analysis will correlate this success with information on the nearby unperturbed frequency positions.

Given the smallness of the isotopic mass perturbations, it is natural to try perturbation theory, the simplest form of which is nondegenerate perturbation theory. With isotopes present, the mass matrix in the mode eigenvalue problem (5) becomes $\boldsymbol{M}_0 + \boldsymbol{\Delta M}$, where $\boldsymbol{M}_0$ corresponds to the unperturbed molecule. As noted above, the force constant matrix remains unperturbed. The derivation of the perturbation series is straightforward, although the problem is slightly different from the usual case based on $(H_0 + V)\psi = E\psi$, because here the perturbation $\boldsymbol{\Delta M}$ is a multiplier of the eigenvalue and also appears in the eigenvector normalization (7). A derivation of the perturbation series for the frequencies which avoids the normalization condition is given in [26]. Here we list the relevant results.

[4] Low-resolution Raman experiments which do not resolve any isotopic structure yield a frequency of 1470 cm^{-1} for the $A_g(2)$ peak, as listed in Table III. The value 1471 cm^{-1} used here corresponds to the $A_g(2)$ mode in $^{12}C_{60}$, which is seen as the high-energy peak in Fig. 3.

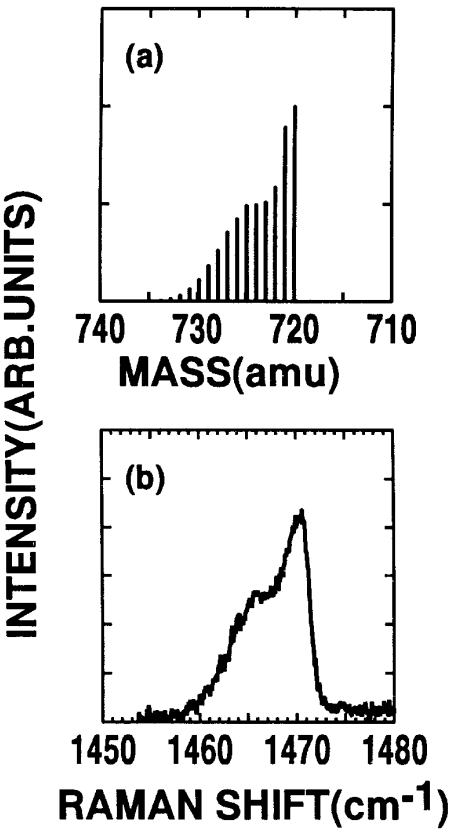

Fig. 4. (a) Mass spectrum of a ^{13}C-enriched C_{60} sample. (b) Unpolarized Raman spectrum of the same enriched sample in CS_2 at 30 K. After *Guha* et al. [21]

The perturbed frequency for a nondegenerate mode f is given by the series

$$\frac{\Delta\omega_f^2}{\omega_{0f}^2} = \sum_{n=1,2,\ldots} \left(\frac{\Delta\omega_f^2}{\omega_{0f}^2}\right)_n , \tag{29}$$

where $\Delta\omega_f^2 \equiv \omega_f^2 - \omega_{0f}^2$ is the shift of the squared frequency of the mode. The first three terms in the right-hand side of this equation are

$$\left(\frac{\Delta\omega_f^2}{\omega_{0f}^2}\right)_1 = -\tilde{\boldsymbol{\chi}}_0(f)\Delta\boldsymbol{M}\boldsymbol{\chi}_0(f), \tag{30}$$

$$\left(\frac{\Delta\omega_f^2}{\omega_{0f}^2}\right)_2 = (\Delta\mathcal{M}_{ff})^2 + \sum_{f'\neq f} \frac{(\Delta\mathcal{M}_{ff'})^2}{1-(\frac{\omega_{0f'}}{\omega_{0f}})^2}, \tag{31}$$

and

$$\begin{aligned}\left(\frac{\Delta\omega_f^2}{\omega_{0f}^2}\right)_3 = &-(\Delta\mathcal{M}_{ff})^3 - 3\Delta\mathcal{M}_{ff}\sum_{f'\neq f}\frac{(\Delta\mathcal{M}_{ff'})^2}{1-(\frac{\omega_{0f'}}{\omega_{0f}})^2} \\ &+\Delta\mathcal{M}_{ff}\sum_{f'\neq f}\frac{(\Delta\mathcal{M}_{ff'})^2}{\left[1-(\frac{\omega_{0f'}}{\omega_{0f}})^2\right]^2} \\ &-\sum_{f',f''\neq f}\frac{\Delta\mathcal{M}_{ff'}\Delta\mathcal{M}_{f'f''}\Delta\mathcal{M}_{f''f}}{\left[1-(\frac{\omega_{0f'}}{\omega_{0f}})^2\right]\left[1-(\frac{\omega_{0f''}}{\omega_{0f}})^2\right]},\end{aligned} \tag{32}$$

where $\Delta\mathcal{M}_{ff'} \equiv \tilde{\boldsymbol{\chi}}_0(f)\Delta\boldsymbol{M}\boldsymbol{\chi}_0(f')$ is the isotope perturbation matrix $\Delta\boldsymbol{M}$, expressed in the basis of unperturbed mode eigenvectors. While just the first two terms are needed in the following, the third-order result is included for reference.

For A_g modes in C_{60} molecules, the first-order shift (30) reduces to a very simple result. Because every site in the unperturbed icosahedral molecule is symmetry equivalent, the magnitudes of the atomic displacements for the unperturbed totally symmetric A_g modes are site-independent, and for the case of n isotopic substitutions $^{12}C \rightarrow {}^{13}C$, (30) gives

$$\left(\frac{\Delta\omega_{A_g}^2}{\omega_{0A_g}^2}\right)_1 = -\frac{n}{720}. \tag{33}$$

This nondegenerate perturbation theory result is independent of the location of the isotopes and is valid provided the unperturbed A_g mode is sufficiently far from the nearby unperturbed modes to which it couples via the perturbation. For the $n = 1$ case of a single isotope, the result is $\Delta\omega_{A_g} = \omega_{0A_g}(\sqrt{719/720}-1)$, and for the unperturbed $A_g(2)$ mode at 1471 cm^{-1}, the predicted shift is -1.02 cm^{-1}, in excellent agreement with the measured shift of -0.98 cm^{-1}.

The above first-order perturbation theory result is also consistent with the strong correlation between the Raman and mass spectrum lineshapes seen in Fig. 4. From (24), the strength of the Raman scattering from mode f is determined by the mode polarizability derivatives $P_{\alpha\beta,f} = \sum_{\ell\gamma} P_{\alpha\beta}(\ell\gamma)\chi(\ell\gamma|f)$. The real-space electronic polarizability derivatives $\{P_{\alpha\beta}(\ell\gamma)\}$ are not changed under isotopic substitution, as noted above, and when first-order perturbation theory is valid, the mode eigenvectors $\{\chi(\ell\gamma|f)\}$ remain unperturbed as well. The Raman intensity for the perturbed A_g mode will then be the same as for the unperturbed molecule. Hence as long as the first-order perturbation theory result (33) remains valid, the Raman spectrum for a mixture of C_{60}

molecules having varying amounts of ^{13}C should simply be proportional to the mass spectrum of the sample, exactly as is seen in Fig. 4.

As the number of isotopes is increased, (33) should eventually fail, but the good agreement just noted implies that the unperturbed $A_g(2)$ mode frequency is relatively isolated from the frequencies of nearby unperturbed modes which can couple appreciably through the mass perturbation. To further explore this question, we also performed nonperturbative calculations of the perturbed normal modes and the associated Raman spectrum. The real-space Raman polarizability derivatives needed for the Raman strengths were obtained from a phenomenological bond-polarizability model which gives an excellent account of the unperturbed C_{60} off-resonance Raman intensities [22], as we detail in Sect. 4.1. For the mode eigenvectors, one can use (5) directly, provided the force constant matrix $\boldsymbol{\Phi}$ is available, either from first-principles or phenomenological models. The resulting mode frequencies and eigenvectors can then be computed for any spatial arrangement of isotopes, and the corresponding Raman spectra predicted. Our results for such calculations, based on the first-principles LDA-based local-orbitals technique discussed in Sect. 1.4, together with the isotopic mixture shown in the top panel of Fig. 4, are given in panel (a) of Fig. 5. The distribution encompasses 0 to 10 ^{13}C isotopes per molecule, and as detailed in [22], the predicted spectra in Fig. 5 include exactly all possible isotopic arrangements for the cases of 0, 1, and 2 ^{13}C isotopes, whereas the cases of 3–10 isotopes are included within an accurate approximation. The agreement between the predicted and observed spectrum is seen to be quite good, although not as good as that found with the simple first-order perturbation theory argument given above, which bypasses detailed model calculations altogether.

Further insight into this problem is obtained by using the corresponding unperturbed mode frequencies and eigenvectors in (31) to evaluate the second-order nondegenerate perturbation theory shifts. The result for the $n = 1$ case of a single isotope is listed in the third column of Table 5, together with the exact nonperturbative shift predicted by our first-principles model, given in the fourth column. As anticipated from the simple first-order nondegenerate perturbation theory results, the second-order shift is significantly smaller than the first-order shift. Nevertheless, it is interesting that the first-order nondegenerate perturbation theory result was in fact essentially perfect, in which case the perturbation theory contributions beyond first order should vanish.

In view of the high accuracy of Giannozzi and Baroni's first-principles Density Functional Perturbation Theory predictions for the frequencies of icosahedral C_{60} [47], displayed here in Table 4, we have repeated our isotopically perturbed Raman spectrum calculations, using their model. The resulting predicted spectrum for the enriched sample of Fig. 4 is shown in panel (b) of Fig. 5, and it is seen to be in very good agreement with the experimental spectrum. The second-order nondegenerate perturbation theory

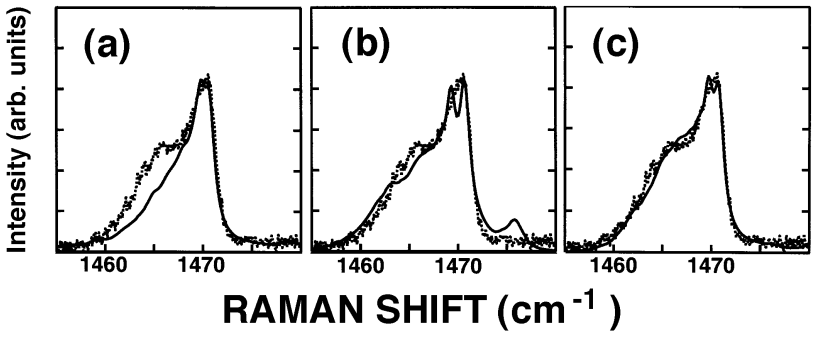

Fig. 5. Solid lines: calculated Raman spectra in the frequency region of $A_g(2)$ for the ^{13}C-enriched C_{60} of Fig. 4. Up to 10 isotopes were included, and the spectra were weighted according to their relative abundances in the mass spectrum. These spectra were calculated nonperturbatively, using the first-principles eigenmodes of [53] for panel (a), the first-principles eigenmodes of [47] for panel (b), and our present frequency assignment of column 2 in Table 4 for panel (c), by implementing (34) in the manner described in the text. The dashed line is the experimental Raman spectrum of Fig. 4b

shift computed using Giannozzi and Baroni's model is given in the second row of Table 5, along with the predicted exact shift. Like our results in the first row, these results are qualitatively consistent with the earlier success of simple first-order nondegenerate perturbation theory, but are quantitatively worse than that simple model-independent prediction.

At this point it is useful to recast the fundamental mode eigenvalue problem (5) into an equivalent form which more transparently brings out the importance of the lineup of unperturbed frequencies. This form is simply obtained by re-expressing (5) in the complete basis of unperturbed orthonormal mode eigenvectors $\{\boldsymbol{\chi}_0(f)\}$. The result is

$$\sum_{f'}[\omega_{0f}^2\delta_{ff'} - \omega_f^2(\delta_{ff'} + \Delta\mathcal{M}_{ff'})]c_{ff'} = 0, \tag{34}$$

where the matrix elements $\Delta\mathcal{M}_{ff'}$ are defined just below (32), and the coefficients $\{c_{ff'}\}$ are the expansion coefficients of the mode eigenvectors in the basis of unperturbed eigenvectors:

$$\boldsymbol{\chi}(f) = \sum_{f'=1}^{3N} c_{ff'}\boldsymbol{\chi}_0(f'). \tag{35}$$

The differences in the predicted isotopically perturbed Raman spectra of panels (a) and (b) of Fig. 5 derive from differences in the mode frequencies and eigenvectors for the two first-principles methods used. We therefore compared the frequencies and eigenvectors for these two models mode by mode

Table 5. Calculated isotopic frequency shifts, in cm^{-1}, for the $A_g(2)$ mode in molecular C_{60} having one ^{13}C atom. The second column gives the shifts predicted by first-order nondegenerate perturbation theory (33), for $n = 1$. They are model-independent. The third column gives the second-order nondegenerate perturbation theory shifts obtained from (31), whereas the fourth column gives nonperturbative shifts. For the first two rows, the indicated models were used, but for the third row $\{\Delta\mathcal{M}_{ff'}\}$ was computed from the unperturbed mode eigenvectors of the LDA-based first-principles calculations of [47], the unperturbed frequencies $\{\omega_{0f}\}$ were taken from our frequency assignment in Table 4, and (34) was used to compute the nonperturbative shifts, as explained in the text. The perturbation theory shifts of the second and third columns were obtained using the experimental Raman frequency $\omega_0 = 1471$ cm^{-1} in the left-hand sides of (30) and (31)

Frequency set	1^{st}-order shift (model independent)	2^{nd}-order shift	Nonperturbative shift
Adams et al.[a]	-1.02	0.21	-0.86
Giannozzi and *Baroni*[b]	-1.02	-0.33	-1.38
Present assignment[c]	-1.02	0.015	-0.97
Experimental shift: -0.98			

[a] Table 4, column 4 (from [53])
[b] Table 4, column 3 (From [47])
[c] Table 4, column 2

and found that while the frequencies differ by as much as 7%, their eigenvectors are practically identical. This distinction between the behavior of the frequencies and eigenvectors in the two models is even more striking when one recalls that the mode eigenvalues are actually the *squares* of the frequencies. Apparently, the very high symmetry of C_{60} imposes rather severe constraints on the forms of the mode displacement patterns. For the isotope problem, this means that the matrix elements $\Delta\mathcal{M}_{ff'}$ appearing in (34) are highly similar in the two models used for panels (a) and (b) of Fig. 5. Hence the dominant contribution to the differences in the two predicted isotopically perturbed spectra derives from the models' different frequency lineups in pure C_{60}.

Moreover, we can use (34) to study easily the effect of our frequency assignment in Table 4 on the isotopically perturbed Raman scattering, even though we have no force constant model underlying these frequencies. This is accomplished by using column 2 of Table 4 for the ω_{0f}'s and simply evaluating the matrix elements $\Delta\mathcal{M}_{ff'}$ using the eigenvectors obtained from either of the above two models. The resulting isotopically perturbed Raman spectrum is given in panel (c) of Fig. 5, and it is in excellent agreement with experiment. In addition, we can use the same $\Delta\mathcal{M}_{ff'}$'s to compute the second-order nondegenerate perturbation theory shift from (31), yielding the result in the third row of Table 5. Now the second-order shift is indeed negligible, as anticipated.

In [22], we performed these approximate, but nonperturbative, calculations of the isotopically perturbed $A_g(2)$ Raman spectrum, for several other published models of the normal modes of pure C_{60}, for which the frequencies, but not the eigenvectors, were available. As shown there, models with unperturbed silent modes having frequencies very close to $A_g(2)$ yield predicted isotopically perturbed spectra which poorly represent the experimental spectrum of Fig. 4(b). Moreover, the predicted shifts are significantly off, and the second-order nondegenerate perturbation contributions turn out to be larger than the first-order corrections. Reference [22] should be consulted for details. Our results demonstrate that this sort of isotopically perturbed Raman scattering study can provide a sensitive probe for quantitative assessments and refinements of theoretical models.

2.6 Inelastic Neutron Scattering

Inelastic neutron scattering (INS) is the most comprehensive technique for the study of vibrations in condensed matter: the $\vec{k}$ conservation and other selection rules are much less restrictive than for optical spectroscopies. In the case of C_{60}, all modes, including those silent for first-order Raman and infrared spectroscopy, can be detected with this technique. The scattering intensity is proportional to the mode degeneracy, a fact that provides a helpful tool for the identification of the vibrations. The primary disadvantage of INS is its poor spectral resolution. This makes it difficult to individually resolve all of the modes, especially when several frequencies are clustered within a narrow range, as is the case for many C_{60} vibrations.

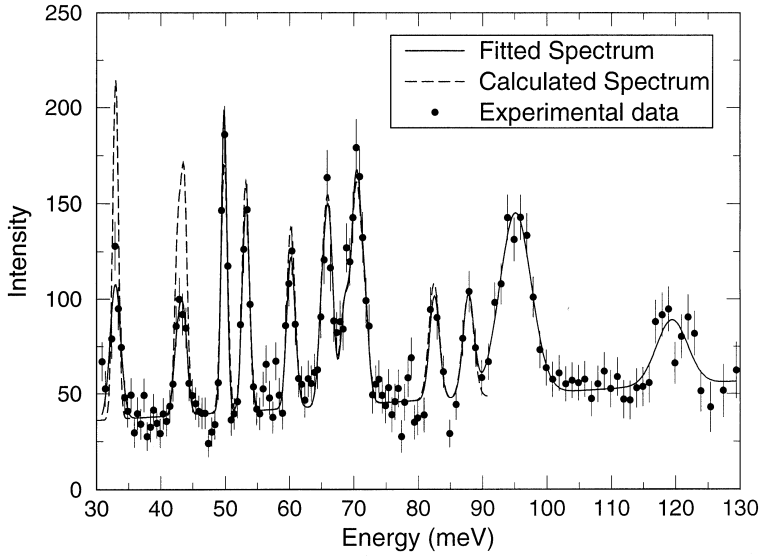

Fig. 6. Measured inelastic neutron scattering spectrum of C_{60}. The solid line shows a fit to a series of Gaussians plus a sloping background. A calculation using frequencies that are virtually identical with those of Table 4 is shown as a solid line. Note that the calculated spectrum ends at 90 meV (730 cm^{-1}). The excellent agreement between the calculation and the Gaussian fit can be extended to 130 meV (1050 cm^{-1}), using the frequencies in Table 4. From [78]

The initial inelastic neutron scattering studies of intramolecular C_{60} modes provided an overall picture of the density of vibrational states and were reasonably consistent with the existent Raman and infrared data, but the resolution was not good enough to identify other modes, particularly in the high energy range [101]. Subsequent work with improved resolution provided the first experimental evidence for several of the assignments in Table 4 [77,102].

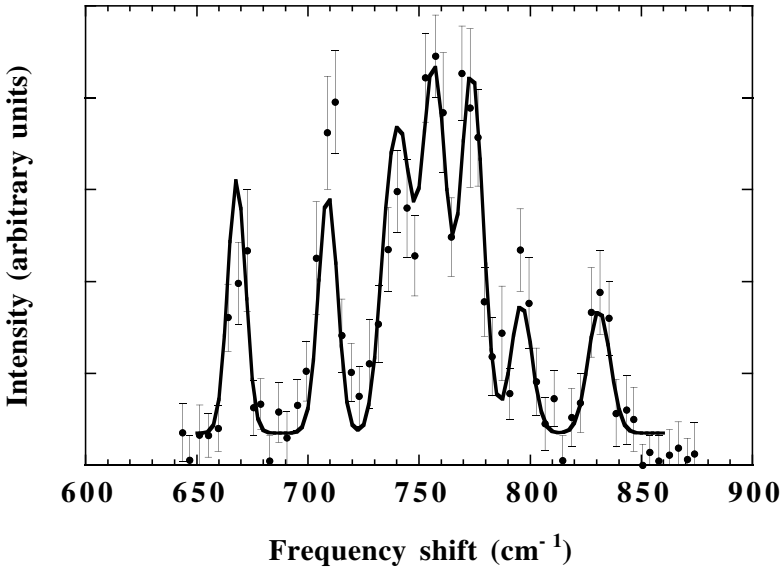

Fig. 7. Experimental inelastic neutron scattering spectrum of C_{60}, showing medium-energy modes (circles) [79]. The solid line is a calculated spectrum consisting of a sum of Gaussians centered at the mode frequencies of Table 4 and weighted according to the modes' degeneracies. The width of each Gaussian is taken to be proportional to the mode's energy and adjusted to the experimental data. The best agreement is obtained using $\Delta E/E = 0.014$. A constant background has been added, and the energies were rescaled as discussed in the text

Prassides et al. [102], for example, identified the $T_{3u}(1)$, $G_u(1)$ and $H_u(1)$ modes. Later work has given a detailed account of all modes below 700 cm^{-1} [40,78]. Figure 6 shows results by *Copley* et al. [78]. The solid line represents a fit to the data with a set of Gaussian functions, whereas the dashed line corresponds to a calculation using mode frequencies that are essentially the same as those in column 2 of Table 4 and in the earlier assignment by *Menéndez* and *Guha* [71]. The agreement between the fit and the calculation is excellent, except for the intensity at the lowest energies, where the discrepancy has been attributed to coherency effects [78].

The agreement between the frequencies of Table 4 and the results of INS extends beyond 700 cm^{-1}. Figures 7 and 8 compare a theoretical prediction based on Table 4 with recent INS data obtained by *Coulombeau* et al. [79]. For this experiment, the authors used the MARI spectrometer at the ISIS pulsed neutron source of the Rutherford Appleton Laboratory, UK. This spectrometer features an array of detectors distributed over a wide angular range, and consequently the momentum transfer $\hbar\vec{Q}$ is not well defined. Since this makes it difficult to include Debye-Waller and coherency effects in the theoretical simulations, we computed each of the theoretical spectra in Figs. 7

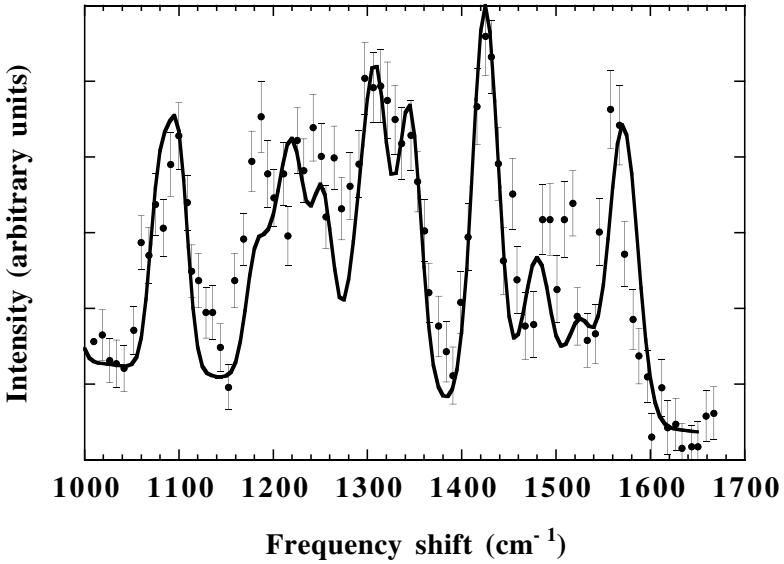

Fig. 8. Experimental inelastic neutron scattering spectrum of C_{60}, showing high-energy modes (circles) [79]. The solid line is a calculated spectrum consisting of a sum of Gaussians centered at the mode frequencies of Table 4 and weighted according to the modes' degeneracies. The width of each Gaussian is taken to be proportional to the mode's energy and adjusted to the experimental data. The best agreement is obtained using $\Delta E/E = 0.022$. A linear background has been added, and the energies were rescaled as discussed in the text

and 8 as a simple sum of Gaussians with weights proportional to the mode degeneracies and a single width parameter $\Delta E/E$ adjusted to best fit the experimental data. The agreement is excellent, and it is made nearly perfect by rescaling the experimental frequencies by a factor of 0.99. This is shown in Figs. 7 and 8. The necessity for the rescaling factor is suggested by the fact that some of the INS peaks which originate from spectroscopically active vibrations appear at an energy 1% higher than the value known from IR or Raman spectroscopy. It is quite apparent that the INS data provide strong support for the mode assignments in Table 4.

2.7 Optical Spectroscopy

Optical absorption spectroscopy, fluorescence and phosphorescence spectra can also be powerful tools for the identification of vibrational modes in molecules. Of particular relevance for our analysis is the work of Sassara et al., who investigated – with exquisite detail – the vibrational fine structure in the fluorescence [80] and phosphorescence [103] spectra of C_{60} molecules isolated in neon and argon matrices. This work leads to the unambiguous identification of several vibrational modes of T_{3u}, H_u, and G_u symmetry.

The major improvements in Table 4 relative to the earlier frequency assignments of *Menéndez* and *Guha* [71] reflect the contribution of the fluorescence experiments.

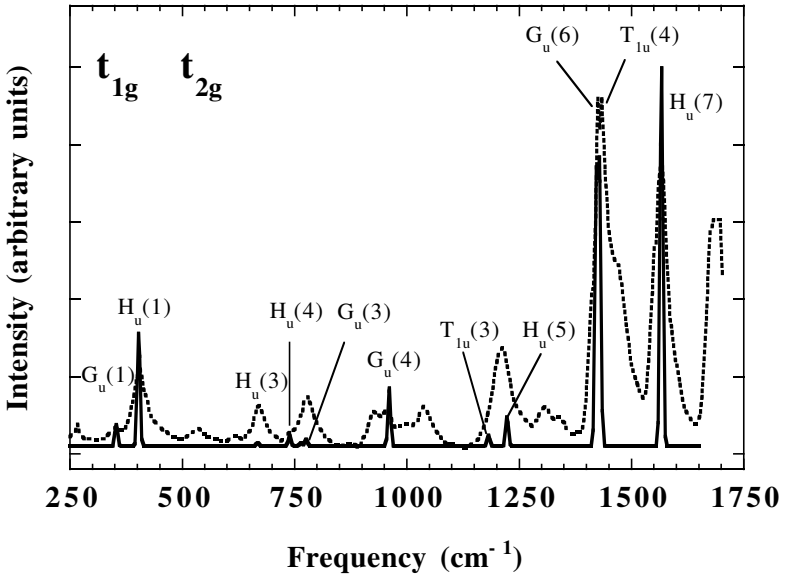

Fig. 9. Experimental fluorescence spectrum of C_{60} in a neon matrix (dashed line) [80]). The frequency scale represents the shift from the origin of the fluorescence. The solid line represents the intensities of Herzberg-Teller modes calculated by *Negri* et al. [107] and plotted according to the mode frequencies in Table 4. The individual peaks in the spectrum were simulated as Gaussians with a FWHM of 7 cm^{-1}. An adjustable parameter was introduced to fit the relative intensities of the t_{1g} and t_{3g} manifolds

According to theoretical calculations [45,104], the three lowest singlet excited states in C_{60} are nearly degenerate and belong to the g_g, t_{3g}, and t_{1g} irreducible representations of the icosahedral group. Here we are using lower-case letters for the primary irreducible representation labels to distinguish electronic from vibrational symmetries. Fluorescence from these states is therefore dipole-forbidden, and the corresponding spectrum is dominated by vibrational bands associated with Herzberg-Teller and Jahn-Teller modes. Since the calculated energy separation between the lowest excited states is very small, the actual lineup of singlet states is likely to be strongly dependent on environmental perturbations. This is confirmed by the experimental work of *Sassara* et al. [80] Figures 9 and 10 show their fluorescence spectra from C_{60} molecules isolated in neon and argon matrices, respectively. The differences in the spectra reflect the different symmetry of the Herzberg-Teller and Jahn-Teller vibrational modes associated with each of the three low-lying singlet

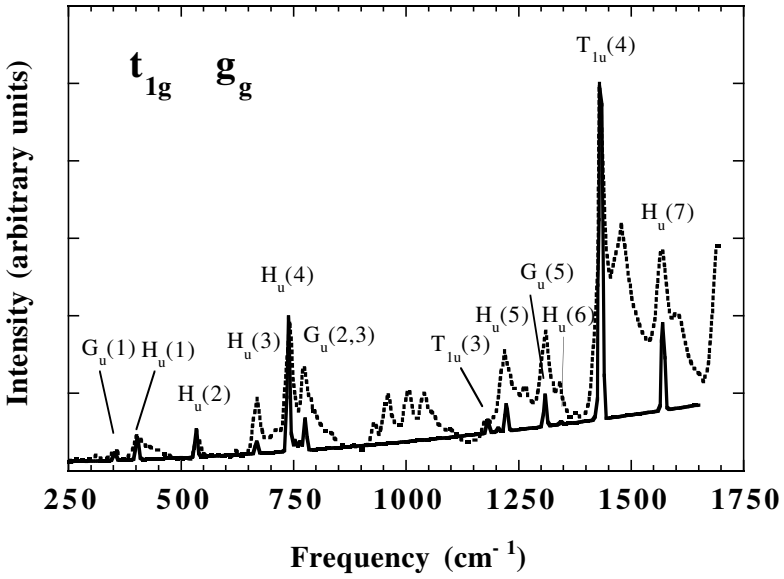

Fig. 10. Experimental fluorescence spectrum of C_{60} in an argon matrix (dashed line, Ref. 40). The frequency scale represents the shift from the origin of the fluorescence. The solid line represents the intensities of Herzberg-Teller modes calculated by *Negri* et al. [107] and plotted according to the mode frequencies in Table 4. The individual peaks in the spectrum were simulated as Gaussians with a FWHM of 7 cm^{-1}. An adjustable parameter was introduced to fit the relative intensities of the t_{1g} and g_g manifolds. A sloping background was also added to improve the agreement between the calculation and the experimental data

states. Active Herzberg-Teller modes are those that couple the lowest singlet states to higher-energy, dipole-allowed t_{1u} states. It is easy to show that the relevant vibrational mode symmetries are H_u and G_u (t_{3g}); A_u, H_u, and T_{1u} (t_{1g}); and H_u, G_u, and T_{3u} (g_g). For Jahn-Teller modes, the symmetries of the active components are H_g (g_g, t_{3g}, and t_{1g}) and G_g (g_g) [105]. These symmetry considerations, combined with calculations of Herzberg-Teller oscillator strengths by *Negri* et al. [105], allowed *Sassara* et al. [80] to explain the fluorescence spectrum from neon matrices as an admixture of t_{1g} and t_{3g} singlet emission. Similarly, the fluorescence spectrum from argon matrices was assigned to a mixture of t_{1g} and g_g emission. From this analysis it is also possible to determine the frequency of several silent modes of H_u, G_u, and T_{3u} symmetry.

The solid lines in Figs. 9 and 10 show the predicted fluorescence intensity based on the Herzberg-Teller calculations of *Negri* et al. [105–107] and our mode frequency assignments from Table 4. The only adjustable parameter in the fit is the relative intensity of the emission from the t_{1g} and t_{3g} states (neon matrices) or t_{1g} and g_g states (argon matrices). It is apparent that the

fluorescence data provide very strong experimental support for many of the assignments in Table 4, most notably for modes $H_u(1)$, $H_u(4)$, $G_u(6)$, and $H_u(7)$.

We indicated above that Table 4 incorporates the fluorescence results through modification of some of the earlier mode assignments made by *Menéndez* and *Guha* [71]. On the other hand, the original frequency assignments in [71] and [72], together with the first-principles normal mode calculations of *Giannozzi* and *Baroni* [47], led to a revised interpretation of some of the details of the fluorescence spectra. This is because *Sassara* et al. based their initial analysis [80] on earlier calculations by *Negri* et al. [105]. A comparison with experimental data that became available after these calculations were published, as well as with the vibrational frequencies of [47], led *Negri* et al. to propose a slightly different assignment of oscillator strengths [106]. Additional discrepancies with the frequency assignments of *Menéndez* and *Guha* [71] motivated yet another revision [107], which has been incorporated into Figs. 9 and 10. It is gratifying to note that the latest calculations of *Negri* et al. [106,107] make it possible to give a unified explanation of the fluorescence and inelastic neutron scattering spectra in terms of the mode frequencies of Table 4.

From the point of view of silent mode spectroscopy, the Herzberg-Teller vibronic activity shown in Figs. 9 and 10 is the most interesting component of the fluorescence. The Jahn-Teller contribution is dominated by Raman-active H_g modes and therefore offers little additional insight into the vibrational structure of C_{60}. However, this contribution must be computed for a detailed quantitative comparison between experimental and theoretical fluorescence spectra, as recently done by *Sassara* et al. [108]. They also included Franck-Condon terms and extended the calculations to take into account two additional many-electron excited states, of t_{3u} and h_g symmetry. The resulting agreement between theory and experiment is very remarkable, with the calculation reproducing the rich fluorescence spectrum, even in its minor details.

2.8 High-Resolution Electron Energy Loss

A beam of monoenergetic electrons is scattered by the electric dipole associated with infrared-active vibrations. This leads to the observation of infrared-active modes in high-resolution electron-energy loss (HREELS) measurements. HREELS experiments require an ultra-high vacuum environment and cannot match the resolution of optical measurements, so that there appears to be no obvious advantage in using this technique for the determination of the infrared mode frequencies. However, HREELS experiments are important for the assignment of vibrational frequencies in C_{60} because *all* modes can induce inelastic scattering of electrons via the short-range components of the electron-molecule interaction. This is the so-called impact scattering

mechanism [109]. *Gensterblum* et al. [109,110] have performed HREELS experiments on C_{60} films. Depending on the substrate used, the films are crystalline or disordered. This has a significant effect on the relative intensity of the different spectral features. Figure 11 shows experimental data for an ordered C_{60} film grown on a GaSe substrate. The spectrum is compared with a broadened density of vibrational states computed from Table 4. It is quite apparent that the mode assignment in Table 4 is consistent with all of the peaks observed with HREELS. The computed density of states also agrees surprisingly well with the peak intensities for the ordered film. The largest discrepancies correspond to the IR active vibrations, which are indicated by arrows in Fig. 11. These discrepancies, however, are not unexpected, since the infrared-active vibrations scatter the electrons via the additional dipole scattering mechanism, which is sensitive to the dipole matrix elements.

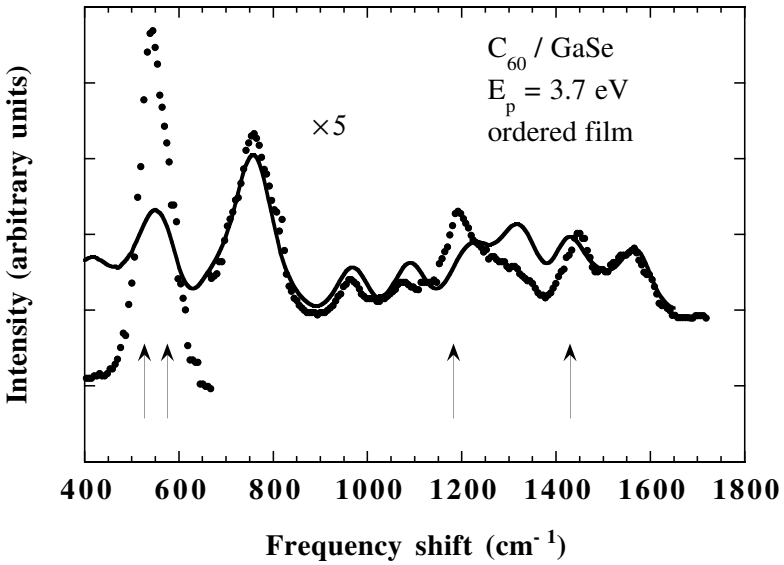

Fig. 11. Experimental HREELS for a C_{60} film grown on GaSe(0001) (points). From Ref. 72. The solid line represents the vibrational density of states in C_{60}, calculated according to the mode frequencies in Table 4. The Gaussian broadening of the density of states was chosen as 70 cm^{-1} (FWHM), which gives an excellent fit of the prominent feature at 758 cm^{-1}. The vertical arrows represent the position of the four T_{1u} modes

According to Table 4, 41 modes (including degeneracies) appear in the 660 cm^{-1}–800 cm^{-1} range. This is consistent with the prominent HREELS peak at 758 cm^{-1}. An equivalent broad structure is apparent in the inelastic neutron scattering spectra. It is noteworthy that within this range there are no infrared-active modes, and the only Raman modes are $H_g(3)$ and $H_g(4)$.

This means that the bulk of the structure is due to silent modes. Similarly, other HREELS peaks can be entirely explained in terms of silent modes. For example, a HREELS peak at 347 cm^{-1} (not shown in Fig. 11) can be identified with the $T_{3u}(1)$ and $G_u(1)$ modes, and the A_u, $T_{3u}(3)$, and $G_u(4)$ modes in Table 4 correspond to the HREELS peak at 960 cm^{-1}.

2.9 Alternative Silent Mode Assignments

Table 4 shows 17 silent modes for which the frequency we recommend cannot be considered definitive. Several of these modes have been given alternative assignments in the literature, which we compile here for completeness. For reasons discussed in Sect. 2.1, we will not consider assignments that deviate from the most accurate first-principles calculations by much more than 5%.

$T_{2u}(2)$

There are two alternative assignments for this mode: an IR peak observed at 709–712 cm^{-1} or an IR peak seen in the range 753–757 cm^{-1} [52,70,73]. The first assignment, favored by *Schettino* et al. [72], is in better agreement with first-principles calculations and is consistent with a weak peak observed at 714 cm^{-1} in fluorescence experiments [80,108]. However, the close proximity of the $H_g(3)$ mode at 709 cm^{-1} makes it difficult to reach definitive spectroscopic conclusions. On the other hand, the IR peak seen in the 753–757 cm^{-1} range cannot be explained as a second-order combination, and it provides, together with our other assignments, the only plausible way to explain the IR peak observed at 2176 cm^{-1} [52,70,73], namely as the combination $H_g(7) + T_{2u}(2)$. Turning to the inelastic neutron scattering data, we note that *Copley* et al. [78] report a peak at 708 cm^{-1}, which is resolution limited, so that if $T_{2u}(2)$ is part of this structure it would have to be almost degenerate with the $H_g(3)$ mode. The intensity of this INS peak is comparable to that of a nearby INS peak at 668 cm^{-1} [78], which corresponds to the 5-fold degenerate $H_u(3)$ mode. Hence, the similar intensity of the 708 cm^{-1} INS peak argues against the existence of both a 5-fold degenerate and a 3-fold degenerate mode at this frequency. Very similar conclusions can be reached from *Coulombeau*'s MARI data [79]. In addition, the higher resolution of this experiment allows the authors to resolve three peaks in the broad structure around 750 cm^{-1}. The theoretical calculation of the INS spectrum agrees better with this three-peak structure if the T_{2u} peak is placed at 753 cm^{-1}, as shown in Fig. 7.

$T_{1g}(2)$

Our assignment of this mode is based on INS data [77,79,102], showing a peak near 840 cm^{-1}. A peak at 813 cm^{-1} has also been reported [70]. Both structures have been assigned to $T_{1g}(2)$ [71,72]. The 840 cm^{-1} assignment

is further supported by a Raman peak observed by *Rosenberg* et al. [89] at 835 cm^{-1} in ^{13}C enriched samples, although this peak can also be assigned to a second-order combination [89]. As can be seen in Fig. 7, the agreement of the MARI INS data of *Coulombeau* et al. [79] with the frequencies in Table 4 is excellent. On the other hand, *Copley* et al. [78] fail to observe any evidence for INS peaks in the 800–900 cm^{-1} range. Moreover, they claim that the strong structure between 725 and 800 cm^{-1} should be assigned to four 3-fold degenerate modes, three 4-fold modes, and two 5-fold modes. This agrees exactly with our assignments if we place the $T_{1g}(2)$ mode below 800 cm^{-1}. We noticed that a frequency of 790 cm^{-1} provides a good fit of the Copley et al. neutron scattering data. However, the latest MARI INS data of *Coulombeau* et al. [79] probably should be preferred in this range, given the better resolution and improved signal-to-noise ratio. This is the reason for our recommended frequency for $T_{1g}(2)$.

$\mathbf{T_{2u}(3)}$

The two first-principles calculations in Table 4 predict three modes in the range 900–1000 cm^{-1}. These are the $G_u(4)$, $T_{2u}(3)$, and A_u modes, and this prediction is in good agreement with INS data. *Copley* et al. [78] find an INS peak at 970 cm^{-1} which has a total integrated intensity consistent with these three modes. The frequency of the $G_u(4)$ mode is 961 cm^{-1} according to the fluorescence experiments [80,108]. We obtain an excellent fit of the INS data of [78] by further assuming that the frequencies of the $T_{2u}(3)$ and A_u modes are 973 cm^{-1} and 984 cm^{-1}, respectively. Unfortunately, the high-resolution MARI INS data of *Coulombeau* et al. [79] do not include this frequency range. Our assignment is also consistent with an observed IR peak at 973 cm^{-1} [70], although this peak can also be explained as a second-order combination. An alternative assignment for $T_{2u}(3)$, proposed by *Schettino* et al. [72], is the IR peak observed at 1040 cm^{-1} [52,72,73], although this peak can also be explained in terms of the second-order combination $H_g(1)+G_u(2)$. No INS structure is seen at this frequency.

$\mathbf{G_g(4)}$

We assigned $G_g(4)$ to a Raman peak observed by several authors at 1079 cm^{-1} [68,86,87,89]. An alternative assignment is a Raman peak seen at 1138–1142 cm^{-1} [68,73,86]. *Gallagher* and coworkers have observed a strong resonance of this peak and have analyzed its excitation profile on the basis of the $G_g(4)$ assignment [111,112]. However, as pointed out by these authors and others, the 1140 cm^{-1} peak can also be explained in terms of the second-order combination $H_g(2)+H_g(3) = 1142$ cm^{-1}. Our assignment of frequencies leads to several more possible combinations: $H_u(1) + H_u(4) = 1142$ cm^{-1}, $T_{1g}(1) + T_{2g}(2) = 1136$ cm^{-1}, $G_g(2)+G_g(2) = 1134$ cm^{-1}, $T_{1g}(1) + G_g(2) = 1135$ cm^{-1}. This would explain the significant width of the 1140

cm^{-1} Raman peak and the observation by *Gallagher* et al. [112] of a shoulder at 1136 cm^{-1}. There are many examples in the literature of second-order Raman peaks which under resonance conditions become stronger than first-order peaks, so we conclude that our assignment of the 1140 cm^{-1} band to a second-order combination is not inconsistent with the existing experimental evidence. Moreover, the INS spectrum shows a pronounced dip at this frequency [79]. Additional work is probably needed to pin down the assignment of $G_g(4)$, but we prefer the assignment in Table 4.

$T_{2u}(4)$, $T_{2u}(5)$ and $G_g(6)$

Our analysis of the isotopic shift of the 1470 cm^{-1} $A_g(2)$ Raman peak shows that the presence of a mode about 12 cm^{-1} higher than this is critical for the explanation of the Raman spectra [21,22]. We placed the $G_g(6)$ mode at this position in view of the theoretical predictions for this mode and the observation of a clear Raman peak at this frequency, which is in fact one of the strongest silent mode signals in the Raman spectrum of C_{60}. As noted earlier, all other G_g modes are seen as weak lines in the Raman spectrum. It was suggested by *Love* et al. [87], however, that the peak at 1482 cm^{-1} corresponds to the $T_{2u}(5)$ mode, and our calculations suggest that this would also be consistent with the observed isotope shifts. The $T_{2u}(5)$ peak has been placed at 1540 cm^{-1} by *Schettino* et al. [72]. We prefer the value 1525 cm^{-1} because it agrees with a weak IR peak [68,70,73], but this peak can also be explained as a second-order combination band. The MARI INS data of *Coulombeau* et al. [79] shows two peaks in this region, which is consistent with the presence of $G_g(6)$ and $T_{2u}(5)$. However, the separation between the two INS peaks is 24 cm^{-1}, whereas according to Table 4 this separation is 43 cm^{-1}. This is one of the only two significant discrepancies between the INS data and Table 4, the other being the position of the highest-energy peak, after rescaling the energies as discussed above. The agreement with the INS data could be improved by placing the T_{2u} peak at 1506 cm^{-1}, but it is uncertain whether the quality of the data guarantees this assignment.

3 Infrared Absorption Intensities of C_{60}

From (17), the area of the first-order IR absorption peak due to mode f is proportional to the square of the dipole moment derivative $\vec{\mu}_f = [\partial\vec{\mu}(\boldsymbol{u})/\partial d_f]_0$. This quantity is determined by the mode eigenvector $\boldsymbol{\chi}(f)$ and the real-space effective charges $[\partial\vec{\mu}(\boldsymbol{u})/\partial u(\ell\alpha)]_0$ through (15) [or its equivalent (18)]. Physically, $\vec{\mu}_f$ is the dipole moment of the system (per unit displacement d_f) after displacing the real-space effective charges according to the mode pattern.

If the adiabatic many-electron ground state wave function $\phi_0(\boldsymbol{x}, \boldsymbol{u})$ is known, the real-space effective charges can be computed directly from the displacement derivatives of (13), and the results combined with calculated mode

Table 6. Electronic-structure based calculations of the relative absorption strengths (peak areas) for the four first-order IR active modes of icosahedral C_{60}. Results are given for three semi-empirical models (TBA and MNDO) and three first-principles models (LDA). The strengths are normalized to that of $T_{1u}(1)$. The last column gives measured values, for comparison

Mode	TBA[a]	TBA[b]	MNDO[c]	LDA[d]	LDA[e]	LDA[f]	Experiment[g]
$T_{1u}(1)$	1.0	1.0	1.0	1.0	1.0	1.0	1.0
$T_{1u}(2)$	0.47	0.08	0.33	0.65	0.65	0.63	0.34
$T_{1u}(3)$	0.17	0.18	1.9	1.4	0.59	0.36	0.28
$T_{1u}(4)$	2.7	1.7	4.4	0.31	0.41	0.57	0.34

[a] *Bertsch* et al. [113]
[b] *Esfarjani* et al. [114]
[c] *Stanton* and *Newton* [43]
[d] *Adams* et al. [53]
[e] *Bertsch* et al. [113]
[f] *Giannozzi* and *Baroni* [47]
[g] *Chase* et al. [84]

eigenvectors to yield predicted IR strengths. Table 6 gives such electronic-structure based predictions, for six representative models. The strengths are normalized to that for $T_{1u}(1)$, and for comparison, the last column gives the strength ratios measured by *Chase* et al. [84]. Columns two and three give results from empirical tight binding models [113,114], the fourth column gives ratios from quantum chemistry semi-empirical MNDO calculations [43], and the results in columns five through seven are from three implementations of first-principles LDA techniques. These are the pseudoatomic orbital scheme [54], which we have previously used to compute the geometries and normal modes of a variety of fullerenes [53] (column five), the Car-Parrinello method [48] as used by *Bertsch* et al. [113] (column six), and Density Functional Perturbation Theory calculations of *Giannozzi* and *Baroni* [47] (column seven). Our choice to compare with the measured IR strength ratios of [84] is somewhat arbitrary, and for comparison, Table 7 lists ratios measured by several groups [84,115–119]. All of these experiments were done on condensed phase samples of C_{60}, either thin film or crystalline, and it is not clear to what extent the differences between the various experiments are due to intermolecular effects, temperature variations, sample/substrate interactions, etc. Since the IR strengths provide a stringent test of theoretical models, it would be very useful to have low temperature IR data available for unperturbed icosahedral C_{60} in the gas phase.

The theoretical IR strength ratios in Table 6 exhibit a wide variation from model to model, much larger than the variations between the different measurements given in Table 7. The mode dipole moment derivatives $\vec{\mu}_f$ describe vibrationally-induced electronic charge redistribution and offer a more diffi-

Table 7. Experimental first-order IR relative strengths. All of the measurements were on thin film samples, except for those of *Winkler* et al. [117], which were on single crystals. Where known, the temperature is listed

	Chase et al.[a]	*Fu* et al.[b]	*Martin* et al.[c]	*Winkler* et al[d] 100K	*Onoe* and *Takeuchi*[e] 300K	*Hara* et al.[f] 90K
$T_{1u}(1)$	1.0	1.0	1.0	1.0	1.0	1.0
$T_{1u}(2)$	0.34	0.39	0.48	0.28	0.30	0.27
$T_{1u}(3)$	0.28	0.29	0.45	0.16	0.22	0.20
$T_{1u}(4)$	0.34	0.36	0.38	0.36	0.24	0.38

[a]Ref. [84]
[b]Ref. [115]
[c]Ref. [116], as quoted in [17]
[d]Ref. [117]
[e]Ref. [118]
[f]Ref. [119]

cult test of electronic-structure based theoretical models than do predictions of either equilibrium geometries or normal modes. Moreover, errors in the $\vec{\mu}_f$'s are magnified when these quantities are squared to form the IR strengths. Although none of the electronic-structure-based calculations yields a highly quantitative reproduction of the measured ratios, the first-principles LDA-based results of columns five to seven are seen to be better qualitatively than those based on empirical electronic structure methods. This is particularly true for the ratios given in columns six and seven, which derive from more exact LDA implementations than we used to obtain the results in column five. In Fig. 12, we compare both the predicted IR frequencies and relative strengths with the experimental values of *Chase* et al. [84], shown in the top panel. The first-principles LDA-based spectrum predicted by *Giannozzi* and *Baroni* [47] is shown in panel (b), and the qualitative agreement with the experimental data is seen to be quite good. Panels (c) and (d) show, respectively, the first-principles LDA-based spectrum of *Adams* et al. [53] and a phenomenological model fit to be discussed below.

The pseudoatomic orbitals LDA scheme [54] that underlies our calculations for panel (c) is convenient for a direct evaluation of the real-space effective charges, since it can be used for an arbitrary atomic configuration. Analogous to our calculation of the force constant matrix, we displace the atom at a given site ℓ successively in the x, y, and z directions by a small amount, while keeping the remaining atoms fixed at their equilibrium positions, and use (13) to calculate the dipole moment of the system, per unit displacement. Provided the displacements are kept small enough that the dipole moment remains linear in the displacements, this yields the 3×3 matrix of real-space effective charges $\{\mu_\beta(\ell\alpha) \equiv [\partial\mu_\beta(\boldsymbol{u})/\partial u(\ell\alpha)]_0 \approx \mu_\beta/u(\ell\alpha)\}$ associated with

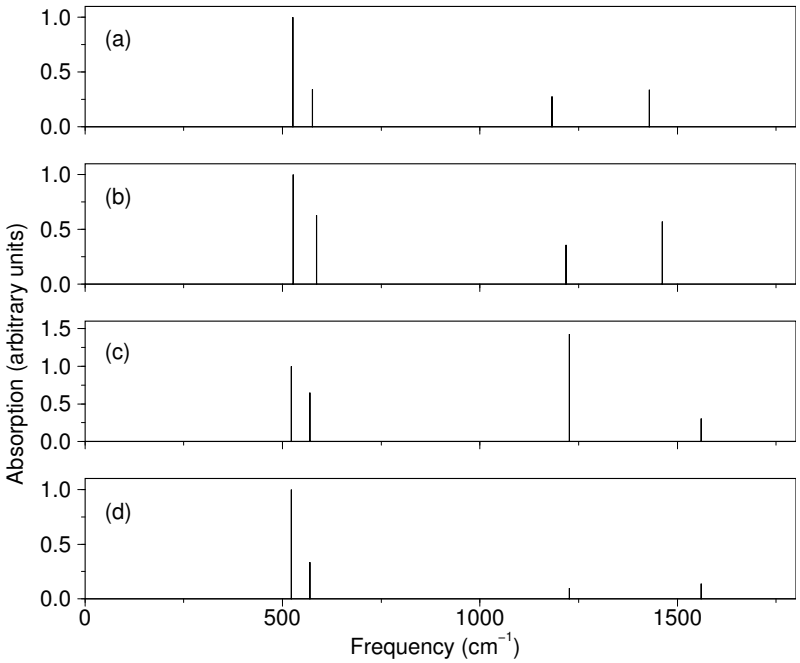

Fig. 12. Measured first-order IR spectra for C_{60}, together with three calculated spectra. The integrated peak intensities are given as vertical lines and are normalized to that for $T_{1u}(1)$. Panel (a) gives the experimental spectrum of *Chase* et al. [84], and panels (b) and (c) give the results of first-principles LDA-based theoretical predictions by *Giannozzi* and *Baroni* [47] and *Adams* et al. [53], respectively. The theoretical spectrum in panel (d) is based on our implementation of the two-parameter phenomenological model of *Fabian* [17]

the site. In practice, this is done for both positive and negative displacements, and the results are averaged to eliminate the nonlinear contributions of even order in the displacements. The resulting effective charges are combined with the mode eigenvectors via (15) to give the $\vec{\mu}_f$'s. While our first-principles strength ratios in Fig. 12 (c) are seen to be in qualitative agreement with the measured values for the second and fourth peaks, the calculated strength for the third peak is almost an order of magnitude too large, despite the fact that our LDA-based method reproduces the experimental C_{60} bond lengths and yields the IR and Raman mode frequencies with an average deviation of better than 4%, as discussed in Sect. 1.4. It is interesting to note that when we apply the same first-principles method to the more complicated C_{70} molecule, which is of D_{5h} symmetry and has 31 symmetry-allowed IR active modes, our results are qualitatively improved with respect to experiment, as will be brought out below.

Given the difficulties of quantitatively predicting IR strengths directly from the electronic states, one can undertake to derive phenomenological models having sufficiently few parameters that the data can be meaningfully fit. If a quantitative model can be achieved, studies of isotope-induced spectral changes can be used to reveal information on spectroscopically inactive modes, as discussed in Sect. 2.5. Moreover, the vast number of possible fullerene structures and the similarity of their local bonding renders them attractive for attempts to develop phenomenological models which can be easily transferred from simpler to more complicated systems.

An ambitious model of this sort is that of *Sanguinetti* et al. [63], which combines the bond charge model of *Weber* [61] with a bond polarizability approach [120,121]. The result is a 6-parameter model which allows one to compute the equilibrium geometry, normal modes, IR strengths, and Raman strengths. The number of independent parameters is reduced to four when first-principles LDA-calculated equilibrium positions are input, and three of these are determined by fitting the frequencies of the 14 first-order IR and Raman modes. The fit reproduces these frequencies with an average deviation of 3.8%. The IR strengths can then be predicted (the Raman strengths require an additional parameter), yielding the strength ratios 1.0, 0.03, 0.4, 0.2. Unfortunately, while the calculated strength ratios for peaks three and four are in qualitative agreement with experiment, the negligible predicted intensity for $T_{1u}(2)$ is strongly at variance with the fact that this is the second most intense measured peak. Moreover, the result of transferring this model to C_{70} in [63] is a predicted IR spectrum which is dominated by a very strong peak near 550 cm^{-1}, whereas the experimental spectrum is dominated by a very intense peak at 1430 cm^{-1}. We do not know how well the situation might be improved by simply using the model to fit the C_{60} IR strengths, at the expense of the mode frequencies. The first-order Raman spectrum predicted by the model for C_{60} is better than for the IR, but the eight H_g peaks are consistently too strong. The predicted Raman spectrum for C_{70} is similarly better than for the IR, although the large number of symmetry-allowed modes (53, encompassing 3 irreducible representations) makes the peak assignments and detailed comparisons difficult.

Since there are many models that give good results for the vibrations, it is reasonable to focus on just the effective charges when trying to develop quantitative phenomenological models for the IR strengths, feeding in the mode eigenvectors from separate calculations. In contrast to bond charge models, which emphasize the effect of the electronic density between the atoms, a simplified classical model for the effective charges which focuses on the π-electron system has been developed by *Fabian* [17]. With the mode eigenvectors given, the result is a two-parameter model for the relative strengths of the first-order IR peaks.

The dipole moment of a given mode in Fabian's model is determined by how the atomic motion affects the classical coordinates $\{\vec{r}_i(t)\}$ of the 60 π

electrons, each of which belongs to a parent carbon atom, at position $\vec{R}_i(t)$. Each carbon is bonded via two "single" bonds and a "double" bond to three neighbors, whose positions are denoted by $\vec{R}_{ij}(t)$, for $j = 1, 3$. Due to the interactions with the three adjacent bonds, the coordinate for π electron i is assumed to vary as $\vec{r}_i(t) = [1 + c_2 \Delta_i(c_1, t)]\hat{n}_i(c_1, t)$, where c_1 and c_2 are the model's fitting parameters, $\hat{n}_i(c_1, t)$ is the unit normal vector to the plane defined by the three neighboring atoms' instantaneous positions (which are rescaled as described below), and $\Delta_i(c_1, t)$ is the difference between the instantaneous and equilibrium values of the distance of the parent atom i from this plane. The dipole moment is simply taken to be $\vec{\mu}(t) = C \sum_{i=1}^{60} \vec{r}_i(t)$, where the constant prefactor C is unimportant for relative intensities. The parameter c_1 accounts in a simplified way for the different interactions between electron i and its adjacent single or double bonds. This is done by rescaling the position of the doubly-bonded neighbor by a factor c_1: $\vec{R}_{id}(t) \rightarrow c_1 \vec{R}_{id}(t)$; no rescaling is done when j represents either of the two singly-bonded neighbors. Geometrically, this rescaling causes the direction of the electron coordinate $\vec{r}_i(t)$ to deviate from the instantaneous normal to the actual plane of neighbors, by instead tilting away (for positive c_1) from the double bond. With just normal mode f excited, the atomic positions are $\vec{R}_i(t) = \vec{R}_{i,0} + \vec{\chi}(i|f)d_f(t)$, and the unit vectors become $\hat{n}_i(c_1, t) = \hat{n}_{i,0}(c_1) + \Delta\hat{n}_i(c_1, t)$, where the zero subscripts denote equilibrium configuration quantities. It is then straightforward to evaluate the mode dipole moment derivatives $\vec{\mu}_f = [\partial\vec{\mu}(\boldsymbol{u})/\partial d_f]_0$ as a function of the atomic equilibrium positions, the mode eigenvectors, and the model parameters c_1 and c_2.

Using our first-principles eigenvectors [53], and varying the parameters c_1 and c_2, we obtain the calculated relative intensities shown in the fourth panel of Fig. 12. Our parameter values are $(c_1, c_2) = (1.34, 0.67)$. These may be compared with the values (1.59, 0.67) obtained by *Fabian* [17], who used a different model for the eigenvectors and fit to the relative intensities measured by *Martin* et al. [116], whereas we are comparing with the data of *Chase* et al. [84]. Although our fit value for the intensity ratio of the first to the second peak is perfect, the third and fourth peaks are roughly a factor of 1/3 too low. Moreover, forcing a better fit for either or both of these two peaks worsens the overall fit. Given that the model has two free parameters for just three observed IR intensity ratios, the results again illustrate the very stringent theoretical test provided by the IR intensities.

The IR intensity model of Fabian is classical and depends only on the geometry of the vibrating molecule, with the central role played by the plane defined by the three neighbors of each carbon atom. To see if the model might have a useful transferability to more complicated trigonally-bonded fullerenes, we used it, with our above values of c_1 and c_2, to compute the relative intensities for D_{5h} C_{70} molecules. These have eight distinct bonds rather than two, and we made the the rough approximation of simply dividing the bonds into two sets, according to whether their lengths are larger or

smaller than 1.425 Å, the midpoint between the measured C_{60} single and double bond lengths. Out of the 31 symmetry-allowed IR active peaks, only 9 are predicted to have intensities greater than 15% of the maximum. This plus the fact that these peaks mainly occur in two frequency regions ($\sim$ 400 cm^{-1}–800 cm^{-1}, and $\sim$ 1200 cm^{-1}–1600 cm^{-1}) are in qualitative agreement with experiment. However, the strongest predicted peaks occur in the first of these regions, whereas the experimental spectrum [122] is dominated by a very intense peak at 1430 cm^{-1}, as noted earlier. Indeed, the overall predicted spectrum is roughly similar to the C_{70} spectrum predicted by Sanguinetti *al.'s* much more complicated bond charge model [63]. It is interesting to note that our fully first-principles calculation of the IR strengths for C_{70} are in good qualitative agreement with experiment, being dominated by a very strong predicted peak at 1532 cm^{-1} [123].

In summary, quantitative theoretical predictions of the first-order IR strengths of C_{60} are challenging for both first-principles and phenomenological models. This is not surprising for the first-principles models, given the sensitivity of the intensities to the electronic states and their matrix elements. Regarding phenomenological approaches, it would be very helpful if a simple model could be developed which easily and reliably transfers between different fullerenes, but such a model does not yet exist. It is interesting that for the presumably more complicated problem of off-resonance Raman intensities, a bond-polarizability model based on a quantitative fit to the observed C_{60} Raman spectrum appears to transfer quite well to more complicated fullerenes, as will be brought out in the next section. These include polymeric fullerenes such as the C_{120} dimer, which include 4-coordinated as well as 3-coordinated atoms. The bond-polarizability model has a total of six parameters (three for each type of bond, single or double), of which five are needed to fit the measured intensity ratios for the ten first-order Raman active modes of C_{60}; thus the model parameters are well-determined by the data, and the question of transferability to other fullerenes can be addressed meaningfully. But for IR spectra, the high symmetry of C_{60} restricts the first-order active modes to only four, and this may be simply too few to pin down the parameters of a realistic and transferable model. Perhaps a better starting point for this purpose would be the richer IR spectrum of the C_{70} molecule.

4 Raman Intensities of C_{60}

Our discussion of Raman intensities begins in Sect. 4.1 with a detailed account of the relative intensities of the 10 first-order peaks observed under off-resonance conditions, where the incident photon energy is well below that of any electronic transition. Section 4.2 concerns the more difficult experimental problem of absolute Raman intensities. Resonance Raman scattering by C_{60}, for which there is still relatively little work, is discussed in Sect. 4.3.

4.1 Relative Intensities for Off-Resonance Scattering

As discussed in Sect. 1.2, the key quantity determining off-resonance Raman intensities is the system's electronic polarizability $\mathcal{P}_{\alpha\beta}(\omega_L, \boldsymbol{u})$ for fixed atomic configuration $\boldsymbol{u}$ and incident light frequency ω_L, where the latter is assumed to be well below any electronic transition frequency. The static limit $\omega_L = 0$ leads to the usual off-resonance selection rules, e.g. for icosahedral C_{60}, the first-order Raman activity is restricted to the A_g and H_g modes. From (24) and (25), the intensity of first-order scattering by mode f is proportional to the square of the mode's static electronic polarizability derivative

$$P_{\alpha\beta,f} = \sum_{\ell\gamma} \left[\frac{\partial \mathcal{P}_{\alpha\beta}(\boldsymbol{u})}{\partial u(\ell\gamma)} \right]_0 \chi(\ell\gamma|f). \tag{36}$$

The dynamical properties enter this quantity through the normal mode eigenvectors $\boldsymbol{\chi}(f)$, while the real-space polarizability derivatives are determined by the electron-vibrational coupling. Section 1.4 reviewed theoretical calculations of C_{60} vibrations, and here we focus on computing the polarizability derivatives.

Just as for the IR effective charges and the dynamical properties, two general approaches can be undertaken to compute the polarizability derivatives $P_{\alpha\beta}(\ell\gamma)$, namely first-principles and phenomenological. For first-principles calculations directly from the basic Born-Oppenheimer electronic states, one could try to use the fundamental linear response theory result (20) for the electronic polarizability. Unfortunately, this would require knowledge of all the many-electron *excited* as well as ground states, and these are very difficult to calculate with current state-of-the-art first-principles techniques. To avoid this, one could instead undertake to solve the many-electron ground state problem in the presence of an applied electrostatic field, with the coupling treated within the dipole approximation, i.e. $-\vec{M}_e \cdot \vec{E}$, where $\vec{M}_e$ is the electronic dipole moment operator $\sum_e q_e \vec{x}_e$. A calculation of the change in the expectation value of $\vec{M}_e$, per unit applied field with the atoms fixed at their equilibrium positions would then yield the static electronic polarizability. To obtain the polarizability *derivatives* would involve the further step of solving the many-electron ground state problem in the presence of both a static E field and a displaced atomic configuration. This is equivalent to computing the *third* derivative of the many-electron ground state energy, twice with respect to an external static electric field and once with respect to an atomic displacement. LDA-based calculation of this sort have been made for small molecules [124,125]. *Giannozzi* and *Baroni* [47] have used Density Functional Perturbation Theory to carry out such calculations for the polarizability derivatives of C_{60}. The resulting Raman peak intensities were not compared with experiment in [47], but they agree quite well with measured first-order off-resonance relative intensities – the theoretical/experimental comparison is shown in Fig. 3 of [126].

Electronic polarizability derivative calculations push first-principles techniques to a more difficult level than do purely vibrational or structural calculations and can become very intensive numerically. Accordingly, phenomenological models are useful. In the previous section we discussed the model of *Sanguinetti* et al. [63], for computing the normal modes, and IR and Raman spectra of C_{60} and C_{70}. In 1993, *Snoke* and *Cardona* [91] combined a simple bond-polarizability model with separate calculations of the vibrations to compute the relative intensities of the first-order Raman lines of C_{60}. We have found this approach to be convenient for studies of isotope effects, as discussed in Sect. 2.5, and for predicting the Raman spectra of more complex structures, such as polymerized fullerenes [53].

The bond polarizability approach was developed for molecules [127], but it is also useful for solid-state applications, as is reviewed in [121]. The basic assumption is that the static electronic polarizability of a covalent system can be written as a sum of contributions from the individual bonds. In its simplest form, the contribution $\Pi_{\alpha\beta}(\vec{R})$ from the bond associated with a pair of atoms separated by $\vec{R}$ is taken to be a cylindrically symmetric function of the bond length. Thus, for a bond parallel to the x-axis, the only nonzero elements of the bond polarizability are $\Pi_{xx}(R) \equiv \alpha_{\parallel}(R)$ and $\Pi_{yy}(R) = \Pi_{zz}(R) \equiv \alpha_{\perp}(R)$. For a general orientation, this becomes

$$\Pi_{\alpha\beta}(\vec{R}) = \frac{R_\alpha R_\beta}{R^2}\alpha_{\parallel}(R) + (\delta_{\alpha\beta} - \frac{R_\alpha R_\beta}{R^2})\alpha_{\perp}(R). \tag{37}$$

The bond polarizability derivatives are then

$$\begin{aligned}\frac{\partial \Pi_{\alpha\beta}(\vec{R})}{\partial R_\gamma} = &\left[\frac{\alpha_{\parallel}(R) - \alpha_{\perp}(R)}{R}\right](\hat{R}_\alpha\delta_{\beta\gamma} + \hat{R}_\beta\delta_{\alpha\gamma} - 2\hat{R}_\alpha\hat{R}_\beta\hat{R}_\gamma) \\ &+\{\alpha'_{\perp}(R)\delta_{\alpha\beta} + [\alpha'_{\parallel}(R) - \alpha'_{\perp}(R)]\hat{R}_\alpha\hat{R}_\beta\}\hat{R}_\gamma,\end{aligned} \tag{38}$$

where $\hat{R}$ is a unit vector along $\vec{R}$.

For (36), we need the derivatives of the system's polarizability with respect to the atomic displacements $\{u(\ell\gamma)\}$, evaluated at the equilibrium configuration. Giving the atom at site ℓ a displacement $\vec{u}(\ell)$ while keeping the remaining atoms fixed, we have $\vec{R}(\ell B) = \vec{R}_0(\ell B) - \vec{u}(\ell)$, where $\vec{R}(\ell B)$ is the bond vector from atom ℓ to any one of its bonded neighbors ℓB, and $\vec{R}_0(\ell B)$ is the corresponding equilibrium configuration bond vector. Then

$$\left[\frac{\partial \mathcal{P}_{\alpha\beta}(\boldsymbol{u})}{\partial u(\ell\gamma)}\right]_0 = -\sum_B{}' \left[\frac{\partial \Pi_{\alpha\beta}[\vec{R}(\ell B)]}{\partial R_\gamma(\ell B)}\right]_0, \tag{39}$$

where the prime over the sum signifies that only the bonds attached to site ℓ are summed. Combining (36), (38), and (39) we can write the mode polar-

izability derivatives in the convenient form [22]

$$P_{\alpha\beta,f} = -\sum_\ell \sum_B' \Bigg[\left\{ \frac{\alpha'_\parallel[R_0(\ell B)]+2\alpha'_\perp[R_0(\ell B)]}{3} \right\} \hat{R}_0(\ell B)\cdot\vec{\chi}(\ell|f)\delta_{\alpha\beta}$$

$$+ \left\{ \frac{\alpha'_\parallel[R_0(\ell B)]-\alpha'_\perp[R_0(\ell B)]}{3} \right\} \Big[3\hat{R}_{0\alpha}(\ell B)\hat{R}_{0\beta}(\ell B) - \delta_{\alpha\beta} \Big] \hat{R}_0(\ell B)\cdot\vec{\chi}(\ell|f)$$

$$+ \left\{ \frac{\alpha_\parallel[R_0(\ell B)]-\alpha_\perp[R_0(\ell B)]}{R_0(\ell B)} \right\} \Big[\hat{R}_{0\alpha}(\ell B)\chi(\ell\beta|f) + \hat{R}_{0\beta}(\ell B)\chi(\ell\alpha|f)$$

$$-2\hat{R}_{0\alpha}(\ell B)\hat{R}_{0\beta}(\ell B)\hat{R}_0(\ell B)\cdot\vec{\chi}(\ell|f) \Big] \Bigg]. \tag{40}$$

The first two terms give the bond-stretching induced changes of the isotropic and anisotropic parts of the bond polarizabilities, respectively, while the third term gives the bond-rotation induced changes of the anisotropic parts of the polarizabilities. For C_{60}, the first term contributes only to the scattering by the two A_g modes, and the other two terms contribute only to the scattering by the eight H_g modes. On a practical note, the above approach is convenient in that it uses the mode eigenvectors in just a single sum over sites, avoiding the need to compute their differences, i.e. the "bond displacements."

Table 8. Parameter ratios for our bond-polarizability model fit to the first-order C_{60} Raman spectrum measured by *Chase* et al. [84] (see footnote 5 on page 59). The incident light frequency used in the experiments was 9398.5 cm^{-1}, below resonance with electronic transitions. The ratios are taken with respect to the quantity $N \equiv [\alpha_\parallel(S) - \alpha_\perp(S)]/R_0(S)$, where S denotes single bonds. Our calculated C_{60} bond lengths are $R_0(S) = 1.45$Å and $R_0(D) = 1.40$Å for single and double bonds, respectively, in agreement with the experimental values. The fit spectra are shown in Fig. 13

Ratio	Fit value
$[\alpha'_\parallel(S) - \alpha'_\perp(S)]/N$	2.80
$[\alpha'_\parallel(S) + 2\alpha'_\perp(S)]/N$	2.73
$[\alpha'_\parallel(D) - \alpha'_\perp(D)]/N$	3.18
$[\alpha'_\parallel(D) + 2\alpha'_\perp(D)]/N$	8.98
$[\alpha_\parallel(D) - \alpha_\perp(D)]/[NR_0(S)]$	0.256

For C_{60}, the bond sum for each site extends over two "single" bonds and one "double" bond, so that there are six independent polarizability parameters, namely $\alpha'_\parallel$, $\alpha'_\perp$, and $\alpha_\parallel - \alpha_\perp$, for each of the two bond types. For the relative intensities of the Raman peaks, only 5 parameters are needed, and

we have fit *Chase* et al.'s [84] off-resonance Raman spectra,[5] normalizing the parameters with respect to $(\alpha_{\parallel} - \alpha_{\perp})/R_0$ for single bonds. Our fit ratios are listed in Table 8, and Fig. 13 gives our calculated spectra. The top panel of the figure shows the measured frequencies and intensities, and the other two panels give the freqencies and intensities computed using the parameters of Table 8 and two different sets of first-principles normal mode frequencies and eigenvectors. For panel (b), we used the eigenfrequencies and eigenvectors of *Giannozzi* and *Baroni* [47], whereas for panel (c) we used those of *Adams* et al. [53]. The actual fitting of the bond polarizability parameters was done using the eigenmodes of [47], but the computed intensities in panels (b) and (c) are seen to be quite similar.

Similar to the IR case, our use of Chase et al.'s experimental off-resonance spectra is somewhat arbitrary, and in Table 9 we compare their intensities with those measured by three other groups. All four experiments were done using 1064 nm incident excitation. The table lists peak heights, since the areas were not reported in every case. All four groups observed a sideband at 266 cm^{-1}, just below the $H_g(1)$ peak. In the data of *Chase* et al. [84], this was reported as a shoulder, but in the other three spectra a separate peak was resolved, whose height is also listed in the table. The shoulder was not included in fitting the data of Chase et al. to obtain the calculated spectrum of Fig. 13(b).

The above bond polarizability approach was discussed in [126], where we explored the extent to which polarizability parameters for small hydrocarbon molecules, namely ethane for the C-C single bonds and ethylene for the double bonds, can be transferred to C_{60} and C_{70}. As noted in Sect. 3, C_{70} is of D_{5h} symmetry and has eight distinct bonds, and we thus made the rough approximation of dividing the bonds into two sets, according to whether their bond lengths are larger or smaller than 1.425 Å, the midpoint between the observed C_{60} single and double bond lengths. The single (double) bond polarizability parameters were then used for bonds in the first (second) set. The use of static hydrocarbon polarizabilities was found to give very good agreement with the measured static polarizabilities for both C_{60} and C_{70}. For the more complicated case of Raman scattering, which is sensitive to the derivatives of the polarizability, the use of hydrocarbon parameters led to only fair agreement with the observed relative intensities for C_{60}, with significant discrepancies occurring for modes above 1000 cm^{-1}. Simply fitting the observed

[5] Note that there is a discrepancy between the peak heights quoted in Table III of [84] and the peak heights shown in Fig. 7 of the same paper. Hence, we obtained the experimental peak areas as follows. First we computed Lorentzian areas by combining the peak heights shown in the experimental spectrum in Fig. 7 of [84] with the peak widths listed in that paper's Table III. We then averaged the resulting areas with those obtained from a second Raman spectrum, kindly sent to us by B. Chase. The averaged peak strengths are shown here as the experimental intensities in Fig. 13, and we obtained our bond polarizability model parameters of Table 8 by fitting these intensities.

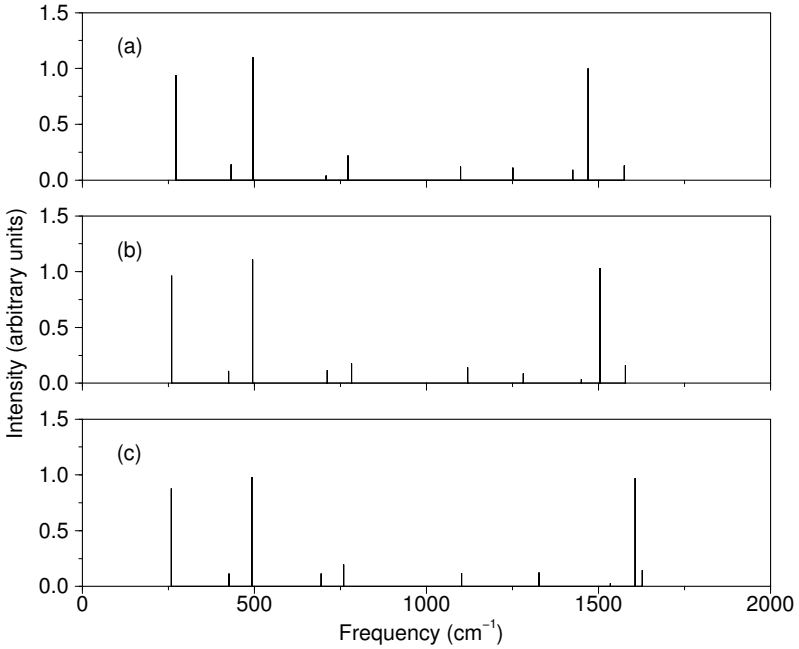

Fig. 13. Measured off-resonance first-order Raman spectra for C_{60}, together with two calculated spectra. The integrated intensities are given as vertical lines. The experimental spectrum of panel (a) is that of *Chase* et al. [84] (see footnote 5 on page 59), measured at $\omega_L = 9398.5$ cm^{-1}. The spectrum of panel (b) was computed using (25) and (40) together with the first-principles normal mode eigenfrequencies and eigenvectors of *Giannozzi* and *Baroni* [47], with the bond polarizability parameters adjusted to fit the measured spectrum of panel (a). The resulting parameter values are given in Table 8. For panel (c), we used these same parameter values, together with the normal mode eigenfrequencies and eigenvectors from the first-principles calculations of *Adams* et al. [53] While absolute intensities were not computed, the vertical scales for panels (b) and (c) are the same, in order to show the effect of the two different sets of mode frequencies and eigenvectors

C_{60} Raman intensities yielded the very good agreement shown here in Fig. 13. Interestingly, for the C_{70} Raman intensities, we found that the use of either the hydrocarbon parameters or the C_{60} fit values yielded comparable qualitatively good agreement with experiment, much better than the hydrocarbon set gave for the C_{60} intensities. It should be noted, though, that the situation for C_{70} is made somewhat difficult by the lack of unambiguous identification of the symmetry types of several of the observed peaks. Nevertheless, given the crudeness of our bond-partitioning scheme described above, the results are encouraging for the transfer of polarizability parameters to more complicated fullerenes. In the papers cited in [53], we have used the same bond partitioning scheme (again with the partitioning bond length of 1.425 Å),

Table 9. Experimental first-order Raman intensities, obtained using incident light from a Nd-YAG laser at 1064 nm. Since the integrated strengths were not reported in each case, but the spectral resolutions were similar, the table gives the measured peak heights obtained directly from the published spectra. The peak heights are normalized to that for the $A_g(2)$ mode. For the $H_g(1)$ peak, the numbers in parentheses give the height of a second peak, observed at 266 cm^{-1} in each of the measured spectra. In the spectra of Chase et al. this peak appears as a shoulder, so no height is listed

	Chase et al.[a]	*Dennis* et al.[b]	*Birkett* et al.[c]	*Lynch* et al.[d]
$A_g(1)$	1.1	0.77	0.65	0.80
$A_g(2)$	1.0	1.0	1.0	1.0
$H_g(1)$	0.91	0.83 (0.21)	0.72 (0.19)	0.96 (0.24)
$H_g(2)$	0.076	0.040	0.056	0.045
$H_g(3)$	0.014	0.011	0.016	0.013
$H_g(4)$	0.18	0.11	0.11	0.13
$H_g(5)$	0.049	0.045	0.035	0.046
$H_g(6)$	0.056	0.046	0.050	0.048
$H_g(7)$	0.013	0.014	0.016	0.017
$H_g(8)$	0.087	0.072	0.098	0.087

[a]Ref. [84]; see footnote 5 on page 59
[b]Ref. [128]
[c]Ref. [129]
[d]Ref. [130]

together with the fit C_{60} bond polarizability parameters of Table 8, to compute the first-order Raman intensities for a variety of polymerized fullerenes. These systems typically contain hundreds of atoms, a few of which are tetragonally rather than trigonally bonded, and they have low symmetry, such that the Raman spectra are quite congested. The use of the fit C_{60} polarizability parameters to predict the Raman spectra of these systems seems a reasonable first approximation, since the spectral congestion is likely to wash out the detailed contributions from individual bonds. We have recently applied this model to new Raman data for the odd-numbered dimeric fullerene C_{119} and have found that it discriminates convincingly between different isomeric configurations [131].

Snoke et al. [132] have likewise studied the question of the transferability of hydrocarbon bond polarizability parameters for computing the first-order off-resonance Raman intensities of C_{60}, using two different force constant models for the normal modes. They also did a pure fit to the observed relative intensities, and some of their fit values of the polarizability parameters differ from those we obtain (Table 8), particularly for $[\alpha_\parallel(D) - \alpha_\perp(D)]/[\alpha_\parallel(S) - \alpha_\perp(S)]$, where the discrepancy is an order of magnitude. The origin of this difference is not known.

4.2 Absolute Raman Cross Sections

Lorentzen et al. [133] have measured the Raman cross-section for the $A_g(2)$ mode (pentagonal pinch) of C_{60}. For an excitation wavelength of 752 nm, they find $d\sigma/d\Omega = (2.09 \pm 0.29) \times 10^{-29}$ cm^2/sr. The measurements were performed on a 4×10^{-4} M solution of C_{60} in CS_2. In such a dilute solution it is reasonable to neglect the effects of C_{60}–C_{60} interactions, so that the measured cross-section can be related to the molecular polarizability derivative occurring in (25). However, we recall that this equation contains no local field corrections, whereas for for C_{60} in CS_2 these corrections should be included. Lorentzen et al. disposed of the local field corrrection by measuring the intensity of the $A_g(2)$ mode relative to that of the the 656 cm^{-1} CS_2 mode and by making the assumption that the local field correction is the same for the two modes. The cross-section for the CS_2 mode was obtained from independent measurements of CS_2/C_6H_6 solutions, taking advantage of the well-known absolute cross-section of the 992 cm^{-1} Raman mode of benzene [134]. Again, the local field corrections were assumed to drop out when taking ratios.

Since the primary motivation of *Lorentzen* et al.'s work [133] was to compare the experimental cross-section with predictions for the off-resonance case, they used the 752 nm line of a Krypton laser instead of the more widely used green-blue lines of an Argon laser. One could go even further below resonance by using the 1064 nm line of a Nd:YAG laser. However, as detailed in [133], CCD detectors have marginal performance in this range. Moreover, there are no well-calibrated absolute Raman intensities available at 1064 nm, whereas at 752 nm it is reasonable to extrapolate the results of *Schomaker* et al. [134] for the 992 cm^{-1} Raman peak of benzene, whose cross-section was determined for excitation wavelengths spanning the visible frequency range down to 656 nm. In this way Lorentzen et al. could avoid having to make a much more difficult *direct* measurement, as would be required for 1064 nm excitation. Thus the choice of 752 nm excitation appears to provide a reasonable compromise between cross-section accuracy and the off-resonance requirement. Using (25) to re-express the measured Raman cross-section in terms of the mode polarizability derivative, one obtains $P_{\alpha\alpha,A_g(2)} = [\partial P_{\alpha\alpha}/\partial d_{A_g(2)}]_0 = (5.66 \pm 0.40) \times 10^{-4}$ cm^2 g$^{-1/2}$. Assuming that the experimental conditions are well below important resonance effects, this value can be compared with predictions of the off-resonance theory, using either the bond polarizability model or *ab initio* calculations.

Bond polarizability models are particularly useful when the polarizability parameters are transferable among different systems, and absolute cross-section measurements provide an additional test of this property. If the transferability hypothesis is approximately correct for fullerenes, as is suggested by the comparison between the measured relative intensities of the first-order Raman peaks and the relative intensities we predict using hydrocarbon polarizability parameters (Fig. 1 in [126]), the error in the calculated absolute cross-section should be comparable to the error in the relative intensities.

This is what *Lorentzen* et al. find [133]. When hydrocarbon polarizability parameters are used, (40) yields $P_{\alpha\alpha,A_g(2)} = 1.7 \times 10^{-4}$ cm^2 g$^{-1/2}$, which is within a factor of 3 of the experimental value.

First-principles methods are expected to make more accurate Raman intensity predictions than simple bond-polarizability models based on the transferability hypothesis. The off-resonance Raman intensities for diamond, silicon and germanium have been calculated by *Windl* [135], using a first-principles approach within the LDA. Excellent agreement with experiment was found for these three materials. As noted earlier, LDA-based methods for the prediction of infrared and Raman activities in small molecules have been investigated in [124] and [125], and for C_{60}, LDA-based calculations of the IR and Raman intensities have been published by *Bertsch* et al. [113] and by *Giannozzi* and *Baroni* [47]. The latter authors' predicted relative intensities for the 10 first-order Raman modes in C_{60} are shown in Fig. 13 and are in very good agreement with experiment. However, the comparison between theoretical and experimental *absolute* cross-sections is not completely straightforward. The calculations of [47] are based on plane wave expansions appropriate to an infinite fcc lattice with periodic boundary conditions, and to focus on the intramolecular properties, an artificially large lattice constant of 16 Å is used. Accordingly, the calculated quantity within this scheme is not the isolated molecular polarizability derivative but the derivative of the "crystalline" dielectric tensor relative to the vibrational normal coordinate. Assuming that the two quantities are related by a Clausius-Mossotti relation, one obtains $P_{\alpha\alpha,A_g(2)} = 2.7 \times 10^{-4}$ cm^2 g$^{-1/2}$, in reasonable agreement with the experimental results [133].

4.3 Resonance Raman Scattering

When the energy of the incident laser photons is well below the lowest absorption edge, the first-order Raman intensities are proportional to the derivatives of the static electronic polarizability with respect to the normal mode displacements. As discussed in Sect. 4.1, these can be computed using either state of the art first principles techniques [47,53] or phenomenological methods [63,91]. However, when the laser excitation energy becomes comparable with that of the electronic absorption bands, the static polarizability approach breaks down. Under these conditions, the individual mode Raman intensities as a function of the exciting laser frequency (Raman excitation profiles) display strong resonance effects [19]. The study of these effects can provide detailed information on the electron-vibration coupling involving specific electronic states and the Raman active modes. Such information is important, for instance, in understanding the superconductivity mechanisms in doped C_{60}.

There are very few detailed experimental studies of Raman excitation profiles in C_{60}, and none of them cover the region between 3 eV and 5 eV, which includes the strongest electronic absorption bands. *Sinha* et al. [136]

carried out resonance Raman experiments in C_{60} films using laser lines in the visible. At room temperature, they found a maximum at 2.4 eV in the Raman excitation profile for the $A_g(2)$ mode. Similar results were obtained by *Matus* et al. [137], but the profile maximum was found to occur at about 2.7 eV. These two experiments were performed on films which contained significant amounts of C_{70}. The existence of a Raman resonance in pure C_{60} films was confirmed by *Guha* et al. [138]. Figure 14 shows the results, which indicate a sharp maximum at 2.3 eV. *Denisov* et al. [139] also report an enhancement of the intensity of the $A_g(2)$ Raman peak, under 488 nm (2.54 eV) excitation from an Argon laser. *Gallagher* et al. [140] compared Raman spectra obtained with the 407 nm and 413 nm lines of a Krypton laser and analyzed them in terms of the so-called "D-term" scattering effects, which arise from non-adiabatic corrections. A few papers have also discussed surface-enhanced Raman scattering in C_{60} [141–143] and the effect of solvents on the Raman intensities [111].

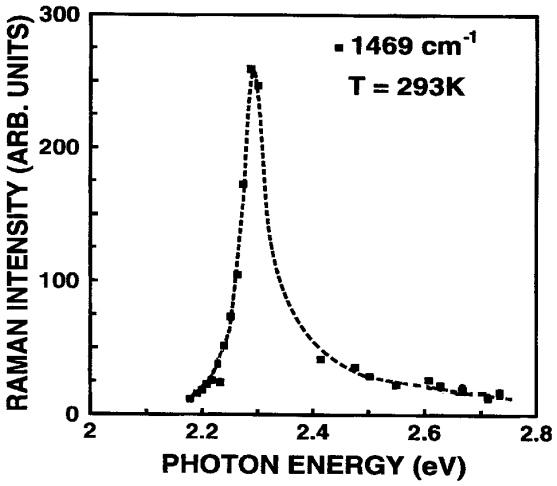

Fig. 14. Raman excitation profile for the $A_g(2)$ mode of C_{60}, from [138] The sample is a polycrystalline film of chromatographically purified material

Two explanations have been offered for the resonance in the excitation profile of the $A_g(2)$ mode in C_{60}. *Sinha* et al. [136] argued that the energy of the resonance was too low to be assigned to optically allowed transitions. Detailed studies of C_{60} in solution show that the first allowed transitions correspond to a broad structure with a maximum at 3.7 eV. The onset of this

structure displays a very weak peak at 3.0 eV [144]. According to theoretical calculations [145], the first allowed transitions involve excited states derived from the h_u (HOMO) and t_{1g} (LUMO+1) molecular orbitals. Thus *Sinha* et al. [136] assigned the observed Raman resonance at 2.4 eV to transitions between crystalline electronic bands derived from the h_u (HOMO) and t_{1u} (LUMO) molecular orbitals. These transitions are optically forbidden in the icosahedral molecule, but it was argued that they should become allowed in the solid state. The mechanism proposed by *Sinha* et al. [136] was supported by the fact that no resonance enhancement was observed in solutions of C_{60} in CS_2. Theoretical calculations of the dielectric function of C_{60} crystals confirmed that "forbidden" HOMO $\rightarrow$ LUMO transitions make a significant contribution to the optical absorption at low energies [146]. Several strong transitions were identified in a range between 0.2 eV and 0.7 eV above the absorption threshold, which was found at 1.46 eV. When the experimental value of 1.72 eV [147,148] is used, these strongest "forbidden" transitions are predicted to occur between 1.9 eV and 2.4 eV, overlapping the energy range within which the Raman resonance was observed by *Sinha* et al. [136] and *Guha* et al. [138]

An alternative explanation for the visible Raman resonance was proposed by *Matus* et al. [137]. These investigators suggested an interpretation based on the "A-term" in *Albrecht*'s molecular theory of resonance Raman scattering [149], with the resonant optical transition occurring between bands derived from the h_u and t_{1g} molecular orbitals. The transition energy between these two levels was placed at 2.7 eV. This is considerably lower than the value of 3.0 eV found for the lowest allowed transition in C_{60} in solution [144], although it is consistent with most absorption and ellipsometric measurements on C_{60} films and single crystals [147,148]. The reason for the discrepancy is now well understood in terms of the width of the electronic bands derived from the molecular orbitals. For example, *Laouini* et al. [150] estimate a separation of 2.9 eV between the h_u (HOMO) and t_{1g} (LUMO+1) levels in the isolated molecule. When the solid is formed, the minimum separation between the energy bands derived from these molecular orbitals is reduced to 2.2 eV. This is consistent with an absorption peak at 3.7 eV (molecule) and 2.7 eV (solid).

Which of these two explanations for the $A_g(2)$ Raman excitation profile is correct remains undecided. *Guha* et al. [138] noted that the Raman resonance could be "turned on" in C_{60} dissolved in CS_2 simply by freezing the solution, suggesting that the Raman resonance is produced by symmetry breaking and not by the particular energy shift of the allowed transitions which occur in the solid state. One could argue, however, that the C_{60} molecule in the frozen solution suffers a perturbation which also lowers the energy of the HOMO $\rightarrow$ LUMO+1 transition, so that *Guha* et al.'s observation [138] is not necessarily inconsistent with *Matus*'s interpretation [137]. One should also keep in mind the possibility that both mechanisms may play a role of comparable sig-

nificance. Unfortunately, the uncertainty as to the relevant electronic states makes it very difficult to analyze the excitation profiles in terms of different theoretical expressions. It is also apparent that deviations from the properties of the isolated molecule, which in the case of the vibrational structure are known to be small, play a key role in determining the measured Raman excitation profiles. This is not surprising when one notes that the Raman studies to date fail to cover the energy range between 3 eV and 5 eV, where the strongest electronic transitions occur and where one might expect a closer similarity between results for isolated molecules and for solid phases.

5 Conclusion

We have presented a survey of the vibrational properties of C_{60} and spectroscopic techniques used to investigate these properties, with the primary emphasis on IR absorption and Raman scattering. It is clear that great progress has been achieved in understanding this unique molecule. The level of detail with which the complex vibrational structure and the spectroscopic intensities are known in C_{60} is unmatched among fullerenes and nanotubes. However, significant gaps remain in this knowledge: some of the silent mode frequencies remain poorly known; the interplay between crystal field effects and isotopic perturbations produces complicated Raman and infrared spectra for which there are often no satisfactory explanations; little evidence exists on the phonon energy bands derived from the intramolecular modes; and while the infrared and off-resonance Raman intensities are reasonably well understood in terms of first-principles and phenomenological models, the information on resonant Raman excitation profiles remains preliminary. We hope that this review will stimulate interest in these topics and further enhance the role of C_{60} as the benchmark system for fullerene studies.

Acknowledgements We would like to thank our collaborators Gary Adams, Stefano Baroni, Paolo Giannozzi, Suchismita Guha, Otto Sankey, and Kislay Sinha, each of whom played key roles in several developments discussed in this chapter. We also benefited from interactions with many colleagues who provided illuminating explanations, unpublished data, and many rounds of useful e-mail discussions. Among these, we would like especially to mention Manuel Cardona, Christian Coulombeau, Bruce Chase, Rolf Heid, Paul Heiney, Herve Jobic, Fabrizia Negri, Dan Neumann, Jun Onoe, and David Snoke. Our work has been supported by the National Science Foundation, under grants DMR 9624102 and DMR 9510182.

References

1. H. W. Kroto, J. R. Heath, S. C. O'Brien, R. F. Curl, R. E. Smalley: Nature **318**, 162 (1985)
2. W. Krätschmer, L. D. Lamb, K. Fostiropoulos, D. Huffman: Nature **347**, 354 (1990)
3. R. C. Haddon, A. F. Hebard, M. J. Rosseinsky, D. W. Murphy, S. J. Duclos, K. B. Lyons, B. Miller, J. M. Rosamilia, R. M. Fleming, A. R. Kortan, S. H. Glarun, A. V. Makhija, A. J. Muller, R. H. Eick, S. M. Zahurak, R. Tycko, G. Dabbagh, F. A. Thiel: Nature **350**, 320 (1991)
4. S. Ijima: Nature **354**, 56 (1991)
5. A. M. Rao, P. Zhou, K.-A. Wang, G. T. Hager, J. M. Holden, Y. Wang, W. T. Lee, X. X. Bi, P. C. Eklund, D. S. Cornet, M. A. Duncan, I. J. Amster: Science **259**, 955 (1993)
6. *Fullerene Polymers and Fullerene Polymer Composites*, ed. by P. C. Eklund, A. M. Rao (Springer, Berlin, Heidelberg), in press
7. W. E. Billups, M. A. Ciufolini: *Buckminster Fullerenes* (John Wiley and Sons, New York, 1993), p. 339
8. D. Koruga, S. Hameroff, J. Withers, R. Loutfy: *Fullerene C_{60}: History, Physics, Nanobiology, Nanotechnology*, (Elsevier Science Ltd., 1993)
9. *Solid State Physics*, ed. by H. Ehrenreich, F. Spaepen (Academic Press, San Diego, 1994), Vol. 48
10. T. Braun, A. Schubert, H. MacZelka, L. Vasvari: *Fullerene Research 1985–1993: A Computer-Generated Cross-Indexed Bibliography of the Journal Literature*, (World Scientific, 1995)
11. M. S. Dresselhaus, G. Dresselhaus, P. C. Eklund: *Science of Fullerenes and Carbon Nanotubes*, (Academic Press, San Diego, 1996)
12. W. Kroto, D. R. M. Walton: *The Fullerenes: New Horizons for Chemistry, Physics, and Astrophysics of Carbon* (Cambridge University Press, London, 1997), p. 154
13. H. Aldersey-Williams: *The Most Beautiful Molecule: The Discovery of the Buckyball*, (John Wiley & Sons, New York, 1995)
14. M. S. Dresselhaus, G. Dresselhaus, P. C. Eklund: J. Raman Spectrosc. **27**, 351 (1996)
15. P. C. Eklund, P. Zhou, K.-A. Wang, G. Dresselhaus, M. S. Dresselhaus: J. Phys. Chem. Solids **53**, 1391 (1992)
16. D. E. Weeks, W. G. Harter: J. Chem. Phys. **90**, 4744 (1989)
17. J. Fabian: Phys. Rev. B **53**, 13864 (1996)
18. M. Tinkham: *Group Theory and Quantum Mechanics*, (McGraw Hill, New York, 1964)
19. See, for instance, J. B. Page: in *Light Scattering in Solids VI*, ed. by M. Cardona, G. Güntherodt (Springer, Berlin, Heidelberg, 1991)
20. G. Placzek: *The Rayleigh and Raman Scattering*, UCRL Translation No. 526(L), from *Handbuch der Radiologie* VI 2 (Akademische Verlagsgsellschaft, Leipzig, 1934), pp. 209–374
21. S. Guha, J. Menéndez, J. B. Page, G. B. Adams, G. S. Spencer, J. P. Lehman, P. Giannozzi, S. Baroni: Phys. Rev. Lett. **72**, 3359 (1994)
22. S. Guha, J. Menéndez, J. B. Page, G. B. Adams: Phys. Rev. B **56**, 15431 (1997)

23. J. D. Axe, S. C. Moss, D. A. Neumann: in *Solid State Physics* ed. by H. Ehrenreich, F. Spaepen (Academic Press, New York, 1994), Vol. 48, p. 149
24. J. E. Fischer, P. A. Heiney: J. Phys. Chem. Solids **54**, 1725 (1993)
25. J. M. Hawkins, A. Mayer, S. Loren, R. Nunlist: J. Am. Chem. Soc. **113**, 9394 (1991)
26. J. Menéndez, J. B. Page, S. Guha: Phil. Mag. B **70**, 651 (1994)
27. Q. Ying, J. Marecek, B. Chu: J. Chem. Phys. **104**, 2665 (1994)
28. P. Launois, S. Ravy, R. Moret: Phys. Rev. B **55**, 2651 (1997)
29. R. M. Fleming, T. Siegrist, P. M. Marsh, B. Hessen, A. R. Kortan, D. W. Murphy, R. C. Haddon, R. Tycko, G. Dabbagh, A. M. Mujsce, M. L. Kaplan, S. M. Zahurak: in *Materials Research Society Symposium*, ed. by R. S. Averback, D. L. Nelson, and J. Bernholc (Materials Research Society, Boston, 1990), Vol. 206
30. P. A. Heiney: J. Phys. Chem. Solids **53**, 1333 (1992)
31. A. B. Harris, R. Sachidanandam: Phys. Rev. B **46**, 4944 (1992)
32. K. Rapcewicz, J. Przystawa: Phys. Rev. B **49**, 13193 (1994)
33. G. Burns, A. M. Glazer: *Space Groups for Solid State Scientists* (Academic Press, New York, 1978), p. 200
34. M. C. Martin, J. Fabian, J. Godard, P. Bernier, J. M. Lambert, L. Mihaly: Phys. Rev. B **51**, 2844 (1995)
35. P. C. Chow, X. Jiang, G. Reiter, P. Wochner, S. C. Moss, J. D. Axe, J. C. Hanson, R. K. McMullan, R. L. Meng, C. W. Chu: Phys. Rev. Lett. **69**, 2943 (1992)
36. S. Ravy, P. Launois, R. Moret: Phys. Rev. B **53**, 10532 (1996)
37. N. Yao, C. F. Klein, S. K. Behal, M. M. Disko, R. D. Sherwood, K. M. Creegan, D. M. Cox: Phys. Rev. B **45**, 11366 (1992)
38. W. I. F. David, R. M. Ibberson, T. J. S. Dennis, J. P. Hare, K. Prassides: Europhysics Lett. **18**, 219 (1992)
39. Z. C. Wu, D. A. Jelski, T. F. George: Chem. Phys. Lett. **137**, 291 (1987)
40. R. Heid, L. Pintschovius, J. M. Godard: Phys. Rev. B **56**, 5925 (1997)
41. L. T. Chadderton: J. Phys. Chem. Solids **54**, 1027 (1993)
42. D. P. Clougherty, J. P. Gorman: Chem. Phys. Lett. **251**, 353 (1996)
43. R. E. Stanton, M. D. Newton: J. Phys. Chem. **92**, 2141 (1988)
44. Z. Slanina, J. M. Rudzinski, M. Togasi, E. Osawa: J. Mol. Struct. **202**, 169 (1989)
45. F. Negri, G. Orlandi, F. Zerbetto: Chem. Phys. Lett. **144**, 31 (1988)
46. S. Baroni, P. Giannozzi, A. Testa: Phys. Rev. Lett. **58**, 1861 (1987)
47. P. Giannozzi, S. Baroni: J. Chem. Phys. **100**, 8537 (1994)
48. R. Car, M. Parrinello: Phys. Rev. Lett. **55**, 2471 (1985)
49. Q. M. Zhang, Jae-Yei Yi, J. Bernholc: Phys. Rev. Lett. **66**, 2633 (1991)
50. G. B. Adams, J. B. Page, O. F. Sankey, K. Sinha, J. Menéndez, D. R. Huffman: Phys. Rev. B **44**, 4052 (1991)
51. A. A. Quong, M. R. Pederson, J. L. Feldman: Solid State Commun. **87**, 535 (1993)
52. X. Q. Wang, C. Z. Wang, K. M. Ho: Phys. Rev. B **48**, 1884 (1993)
53. G. B. Adams, J. B. Page, O. F. Sankey, M. O'Keeffe: Phys. Rev. B **50**, 17471 (1994); G. B. Adams, J. B. Page, O. F. Sankey, M. O'Keeffe: Chem. Phys. Lett. **228**, 485 (1994); G. B. Adams, J. B. Page: in [6]
54. O. F. Sankey, D. Niklewski: Phys. Rev. B **40**, 3979 (1989); O. F. Sankey, D. J. Niklewski, D. A. Drabold, J. D. Dow: Phy. Rev. B **41**, 12750 (1990)

55. G. B. Adams, O. F. Sankey, J. B. Page, D. Drabold: Science **256**, 1792 (1992)
56. J. Harris: Phys. Rev. B **31**, 1770 (1985)
57. O. F. Sankey, R. E. Allen: Phys. Rev. B **33**, 7164 (1986)
58. B. P. Feuston: Phys. Rev. B **44**, 4056 (1991)
59. R. A. Jishi, R. M. Mirie, M. S. Dresselhaus: Phys. Rev. B **45**, 13685 (1992)
60. J. L. Feldman, J. Q. Broughton, L. L. Boyer, D. E. Reich, M. D. Kluge: Phys. Rev. B **46**, 12731 (1992)
61. W. Weber: Phys. Rev. B **15**, 1789 (1977)
62. G. Onida, G. Benedek: Europhysics Lett. **18**, 403 (1992)
63. S. Sanguinetti, G. Benedek, M. Righetti, G. Onida: Phys. Rev. B **50**, 6743 (1994)
64. K.-P. Bohnen, R. Heid, K. M. Ho, C. T. Chan: Phys. Rev. B **51**,5805 (1995)
65. W. Que, M. B. Walker: Phys. Rev. B **48**, 13104 (1993)
66. J. Yu, R. K. Kalia, P. Vashishta: Appl. Phys. Lett. **63**, 3152 (1993)
67. J. M. Pacheco, J. P. P. Ramalho: Phys. Rev. Lett. **79**, 3873 (1997)
68. Z.-H. Dong, P. Zhou, J. M. Holden, P. C. Eklund, M. S. Dresselhaus, G. Dresselhaus: Phys. Rev. B **48**, 2862 (1993)
69. K.-A. Wang, A. M. Rao, P. C. Eklund, M. S. Dresselhaus, G. Dresselhaus: Phys. Rev. B **48**, 11375 (1993)
70. M. C. Martin, X. Du, J. Kwon, L. Mihaly: Phys. Rev. B **50**, 173 (1994)
71. J. Menéndez, S. Guha: in *22nd International Conference on the Physics of Semiconductors*, ed. by D. Lockwood (World Scientific, Vancouver, Canada, 1994), p. 2093
72. V. Schettino, P. R. Salvi, R. Bini, G. Cardini: J. Chem. Phys. **101**, 11079 (1994)
73. P. Bowmar, W. Hayes, M. Kurmoo, P. A. Pattenden, M. A. Green, P. Day, K. Kikuchi: J. Phys.: Condens. Matter **6**, 3161 (1994)
74. L. Akselrod, H. J. Byrne, S. Donovan, S. Roth: Chem. Phys. **192**, 307 (1995)
75. W. Brockner, F. Menzel: J. Mol. Struct. **378**, 147 (1996)
76. A. Graja, A. Lapinski, S. Król: J. Mol. Struct. **404**, 147 (1997)
77. C. Coulombeau, H. Jobic, P. Bernier, C. Fabre, D. Schütz, A. Rassat: J. Phys. Chem. **96**, 22 (1992)
78. J. R. D. Copley, D. A. Neumann, W. A. Kamitakahara: Can. J. Phys. **73**, 763 (1995)
79. C. Coulombeau, H. Jobic, C. J. Carlile, S. M. Bennington, C. Fabre, A. Rassat: Fullerene Science and Technology **2**, 247 (1994)
80. A. Sassara, G. Zerza, M. Chergui: J. Phys. B **29**, 4997 (1996)
81. W. Kraetschmer, K. Fostiropoulos, D. R. Huffman: Chem. Phys. Lett. **170**, 167 (1990)
82. D. S. Bethune, G. Meijer, W. C. Tang, H. J. Rosen, W. G. Golden, H. Seki, C. A. Brown, M. S. de Vries: Chem. Phys. Lett. **179**, 181 (1991)
83. R. Liu, M. V. Klein: Phys. Rev. B **45**, 11437 (1992)
84. B. Chase, N. Herron, E. Holler: J. Phys. Chem. **96**, 4262 (1992)
85. K. Sinha, J. Menéndez, G. B. Adams, J. B. Page, O. F. Sankey, L. D. Lamb, D. R. Huffman: in *Appl. Spectr. in Materials Science*, ed. by D. D. Saperstein (SPIE, Los Angeles, 1991) Vol. 1437, p. 32
86. P. H. M. van Loosdrecht, P. J. M. van Bentum, M. A. Verheijen, G. Meijer: Chem. Phys. Lett. **198**, 587 (1992)
87. S. P. Love, D. McBranch, M. Salkola, N. V. Coppa, J. M. Robinson, B. I. Swanson, A. R. Bishop: Chem. Phys. Lett. **225**, 170 (1994)

88. L. Yulong, J. Yijian, L. Jingqing, M. Yujun, X. Sishen, Z. Zebo, Q. Shengfa: Phys. Rev. B **49**, 5058 (1994)
89. A. Rosenberg, C. Kendziora: Phys. Rev. B **51**, 9321 (1995)
90. J. Menéndez, J. B. Page: Bull. Am. Phys. Soc. **43**, 157 (1998)
91. D. W. Snoke, M. Cardona: Solid State Commun. **87**, 121 (1993)
92. M. Matus, H. Kuzmany: Appl. Phys. A **56**, 241 (1993)
93. P. H. M. van Loosdrecht, P. J. M. van Bentum, J. Meijer: Phys. Rev. Lett. **68**, 1176 (1992)
94. C. C. Homes, P. J. Horoyski, M. L. W. Thewalt, B. P. Clayman: Phys. Rev. B **49**, 7052 (1994)
95. C. C. Homes, P. J. Horoyski, M. L. W. Thewalt, B. P. Clayman, T. R. Anthony: Phys. Rev. B **52**, 16892 (1995)
96. P. J. Horoyski: Phys. Rev. B **54**, 920 (1996)
97. L. Pintschovius, B. Renker, F. Gompf, R. Heid, S. L. Chaplot, M. Haluska, H. Kuzmany: Phys. Rev. Lett. **69**, 2662 (1992)
98. S. A. Fitzgerald, A. J. Sievers: Phys. Rev. Lett. **70**, 3175 (1993)
99. P. J. Horoyski, M. L. W. Thewalt: Phys. Rev. B **48**, 11446 (1993)
100. P. J. Horoyski, M. L. W. Thewalt, T. R. Anthony: Phys. Rev. B **52**, R6951 (1995)
101. R. L. Cappelletti, J. R. D. Copley, W. A. Kamitakahara, F. Li, J. S. Lannin, D. Ramage: Phys. Rev. Lett. **66**, 3261 (1991)
102. K. Prassides, T. J. S. Dennis, J. P. Hare, J. Tomkinson, H. W. Kroto, R. Taylor, D. R. M. Walton: Chem. Phys. Lett. **187**, 455 (1991)
103. A. Sassara, G. Zerza, M. Chergui: Chem. Phys. Lett. **261**, 213 (1996)
104. I. Laszlo, L. Udvardi: Chem. Phys. Lett. **136**, 418 (1989)
105. F. Negri, G. Orlandi, F. Zerbetto: J. Chem. Phys. **97** 6496 (1992)
106. F. Negri, G. Orlandi, F. Zerbetto: J. Phys. Chem. **100**, 10849 (1996)
107. F. Negri: Private communication
108. A. Sassara, G. Zerza, M. Chergui, F. Negri, G. Orlandi: J. Chem. Phys. **107**, 8731 (1997)
109. G. Gensterblum, L.-M. Yu, J.-J. Pireaux, R. Caudano, J.-M. Themlin, S. Bouzidi, F. Coletti: Appl. Phys. A **56**, 175 (1993)
110. G. Gensterblum, J. J. Pireaux, P. A. Thiry, R. Caudano, J. P. Vigneron, P. Lambin, A. A. Lucas, W. Krätschmer: Phys. Rev. Lett. **67**, 2171 (1991)
111. S. H. Gallagher, R. S. Armstrong, P. A. Lay, C. A. Reed: Chem. Phys. Lett. **248**, 353 (1996)
112. S. H. Gallagher, R. S. Armstrong, W. A. Clucas, P. A. Lay, C. A. Reed: J. Phys. Chem. A **101**, 2960 (1997)
113. G. F. Bertsch, A. Smith, K. Yabana: Phys. Rev. B **52**, 7876 (1995)
114. K. Esfarjani, Y. Hashi, J. Onoe, K. Takeuchi, Y. Kawazoe: Phys. Rev. B **57** 223 (1998)
115. K.-J. Fu, W. L. Karney, O. L. Chapman, S.-M. Huang, R. B. Kaner, F. Diederich, K. Holczer, R. L. Whetten: Phys. Rev. B **46** 1937 (1992)
116. M. C. Martin, D. Koller, L. Mihaly: Phys. Rev. B **47** 14607 (1993)
117. R. Winkler, T. Pichler, H. Kuzmany: Zeit. Phys. B **96**, 39 (1994)
118. J. Onoe, K. Takeuchi: Phys. Rev. B **54**, 6167 (1996), as reported in [114]
119. T. Hara, J. Onoe, K. Takeuchi: J. Phys. Chem. B **101**, 9532 (1997)
120. S. Go, H. Bilz, M. Cardona: Phys. Rev. Lett. **34**, 580 (1975)
121. H. Bilz, D. Strauch, R. K. Wehner: *Handbuch der Physik* (Springer-Verlag, Berlin, 1984), Vol. XXV, Pt. 2d, p. 253

122. A. von Czarnowski, K. H. Meiwes-Broer: Chem. Phys. Lett. **246**, 321 (1995)
123. G. B. Adams, J. B. Page: unpublished
124. B. G. Johnson, J. Florián: Chem. Phys. Lett. **247**, 120 (1995)
125. D. Porezag, M. R. Pederson: Phys. Rev. B **54**, 7830 (1996)
126. S. Guha, J. Menéndez, J. B. Page, G. B. Adams: Phys. Rev. B **53**, 13106 (1996)
127. M. Wolkenstein: Dokl. Akad. Nauk. SSSR **32**, 185 (1941)
128. T. J. Dennis, J. P. Hare, H. W. Kroto, R. Taylor, D. R. M. Walton: Spectrochim. Acta **47A**, 1289 (1991)
129. P. R. Birkett, H. W. Kroto, R. Taylor, D. R. M. Walton, R. I. Grose, P. J. Hendra, P. W. Fowler: Chem. Phys. Lett. **205**, 399 (1993)
130. K. Lynch, C. Tanke, F. Menzel, W. Brockner, P. Scharf, E. Stumpp: J. Phys. Chem. **99**, 7985 (1995)
131. S. Lebedkin, H. Rietschel, G. B. Adams, J. B. Page, W. E. Hull, F. H. Hennrich, H.-J. Eisler, M. M. Kappas, W. Krätschmer: J. Chem. Phys. **110**, 11768 (1999)
132. D. W. Snoke, M. Cardona, S. Sanguinetti, G. Benedek: Phys. Rev. B **53**, 12641 (1996)
133. J. Lorentzen, S. Guha, J. Menéndez, P. Giannozzi, S. Baroni: Chem. Phys. Lett. **270**, 129 (1997)
134. K. T. Schomacker, J. K. Delaney, P. M. Champion: J. Appl. Phys. **85**, 4241 (1986)
135. W. Windl: *Ab-initio-Berechnung von Raman-Spektren in Halbleitern*, Doctoral dissertation, University of Regensburg, Germany, 1995.
136. K. Sinha, J. Menéndez, R. C. Hanson, G. B. Adams, J. B. Page, O. F. Sankey, L. D. Lamb, D. R. Huffman: Chem. Phys. Lett. **186**, 287 (1991)
137. M. Matus, S. Balgavy, H. Kuzmany, and W. Krätschmer: *Resonance Raman Spectroscopy of Buckminsterfullerene*, Physica C **185–189**, 423 (1991)
138. S. Guha, J. Lorentzen, K. Sinha, J. Menéndez, G. B. Adams, J. B. Page, O. F. Sankey: Mol. Cryst. Liq. Cryst. **256**, 391 (1994)
139. V. N. Denisov, B. N. Mavrin, G. Ruani, R. Zamboni, C. Taliani: Sov. Phys. JETP **75**, 158 (1992)
140. S. H. Gallagher, R. S. Armstrong, P. A. Lay, C. A. Reed: J. Am. Chem. Soc. **116**, 12091 (1994)
141. K. L. Akers, L. M. Cousins, M. Moskovits: Chem. Phys. Lett. **190**, 614 (1992)
142. A. Rosenberg: Phys. Rev. B **51**, 1961 (1995)
143. X. Andong, P. Haibin, Z. Xinyi, H. Yilin, F. Shaojun, S. Junyan, Z. Jian, X. Cunyi: J. Lumin. **63**, 301 (1995)
144. S. Leach, M. Vervloet, A. Desprès, E. Brèheret, J. P. Hare, T. J. Dennis, H. W. Kroto, R. Taylor, D. R. M. Walton: Chem. Phys. **160**, 451 (1992)
145. S. Larsson, A. Volosov, A. Rosén: Chem. Phys. Lett. **137**, 501 (1987)
146. W. Y. Ching, M.-Z. Huang, Y.-N. Xu, W. G. Harter, F. T. Chan: Phys. Rev. Lett. **67**, 2045 (1991)
147. Y. Wang, J. M. Holden, A. M. Rao, W.-T. Lee, X. X. Bi, S. L. Ren, G. W. Lehman, G. T. Hager, P. C. Eklund: Phys. Rev. B **45**, 14396 (1992)
148. P. Milani, M. Manfredini, G. Guizzetti, F. Marabelli, M. Patrini: Solid State Commun. **90**, 639 (1994)
149. A. C. Albrecht: J. Chem. Phys. **34**, 1476 (1961)
150. N. Laouini, O. K. Andersen, O. Gunnarson: Phys. Rev. B **51**, 17446 (1995)